The Pennsylvania State University

The Graduate School

College of Earth and Mineral Sciences

GEOPRESSURE AND FLOW FOCUSING ON THE SLOPE OF THE GULF OF MEXICO, GC 65

A Thesis in

Geosciences

by

Jacek Andrzej Lupa

Submitted in Partial Fulfillment
of the Requirements
for the Degree of

Master of Science

May 2002

I grant The Pennsylvania State University the non-exclusive right to use this work for the University's own purposes and to make single copies of the work available to the public on a not-for-profit basis if copies are not otherwise available.

_____

Jacek Lupa

We approve the thesis of Jacek Andrzej Lupa.

Date of Signature

_____ _____

Peter B. Flemings

Associate Professor of Geosciences

Thesis Advisor

_____ _____

Derek Elsworth

Professor of Energy and Geo-Environmental Engineering

_____ _____

Rudy L. Slingerland

Professor of Geology

_____ _____

Peter Deines

Professor of Geochemistry

Associate Head for Graduate Programs and Research

Abstract

At Green Canyon 65, on the slope of the Gulf of Mexico, rapid deposition of low permeability Pleistocene sediments has resulted in overpressures originating near the seafloor and increasing at near lithostatic gradients with depth. In the Bullwinkle mini-basin, characterization of sand and shale overpressures, using *in situ* data and wireline prediction, suggest sand and salt geometry play a role in overpressure distribution and magnitude. Three 2- and 3-D steady-state flow models are developed to account for the overpressure and flow phenomena that occur around the J-Sands, a bowl shaped turbidite sand package located at 3350 m depth. The models illustrate the effect of sand and salt geometry on sand overpressure, and suggest that an impermeable salt layer beneath the J Sand is controlling overpressure in both the sand and the Bullwinkle basin.

The flow focusing model is then applied to a trap integrity case study in GC 64. As pressure converges on the least principal stress, processes such as shear failure or hydrofracture may generate fracture permeability. This enhanced permeability facilitates the expulsion of hydrocarbons from a reservoir. In the J Boxer sand, pressure at the top of the hydrocarbon column is within 2.5 MPa of the maximum principal stress (S_v). Seismic evidence suggests that gas is being expelled from the top of the sand. I describe with an analytical flow model how flow focusing has elevated pressure at the top of structure to within 1 MPa of the minimum principal stress (S_{hmin}). I then discuss the implication of flow focusing for prospect evaluation and for estimating trap integrity before drilling.

Contents

List of Figures

List of Tables

Acknowledgements

Numerous individuals that have helped shape my graduate and academic career. Of course those most directly responsible for my successes thus far have been my family whom I cannot thank enough for their support. I am forever indebted to my parents for their sacrifices and their selflessness that gave me many incredible opportunities. My brother, Michal, I'd like to thank for his encouragement, his friendship and for helping define myself as a person. I'd like to thank Alyson Becker for her patience, understanding and for making me happier than I could ever imagine by myself.

From the onset, the people of the Basin Research Group made the transition into graduate life a successful one. The support, advice and direction that my advisor, Dr. Peter Flemings, provided were invaluable. His enthusiasm, drive and dedication cannot be understated. Brandon Dugan's (B Diddy) technical expertise, ideas and deep understanding of fluid flow helped to shape and refine my thesis. Rachel Altemus and Heather Johnson made my graduate career flow smoothly, solving all of my little dilemmas and making sure I had all the resources I needed. Without these people, this thesis could not have come to fruition.

The richness, fullness and success of my graduate career at Penn State would not have been possible without all the people of the Deike Building. I'd especially like to thank all the friends that I've made over the past several years for making my time here a happy

one, socially and academically. I particularly thank the GeoSystems team, Alastair (Swanny), Joe (Commander) and Kevin (Kev-e-Kev), for the help on Bullwinkle and the friendship they provided. The crack computer team of John Miley and Tom Canich were indispensable. Dr. Rudy Slingerland and the Geohabs also deserve special mention for providing me the opportunity to continue living out my NHL dreams.

Finally, my academic career would not have been possible without the funding of the Penn State GeoFluids Consortium and the Exxon Quantitative Geosciences Fellowship. The majority of the data used in my studies were provided by Shell Exploration and Production Company (SEPCo) as part of the Penn State Geosystems Initiative. I'd like to thank all the members of the consortium, in particular Phillips Petroleum, who provided me with an internship and much needed training. Also several key individuals gave me some incredibly useful insight and opportunities, including Bill Kilsdonk, Mike Mahler, Glenn Bowers and Bob Bruce.

Chapter 1: Introduction

1.1. Background

Flow focusing occurs when a dipping, hydrologically continuous sand lies between much lower permeability, overpressured shales. In this environment, the vertical pressure gradient in the sand is approximately hydrostatic, whilst the pressure gradient in the shale is typically near the lithostatic gradient. Because of the difference in gradients, sand pressure at the top of the structure is elevated with respect to the surrounding shale, and pressure low on the structure is depressed. The pressure difference between the sand and shale low and high on the structure results in the focusing of flow through the permeable sand.

The groundwork for the flow focusing model was introduced by Traugott (1996). Traugott (1996) noticed that around dipping, permeable sand lenses, the sand and shale had different pressure gradients. Initial attempts to explain this behavior focused upon static influences such as loading geometry as the key attribute (Stump & Flemings, 2000). Overpressure in the shale was expressed as a function of the overlying load. The overpressure in the sand simply equaled the average shale overpressure bounding the sand.

The dynamic behavior of the system was considered to describe the role of permeability and fluid flow on the overpressure field (Stump & Flemings, 2000; Yardley & Swarbrick,

2000; Dugan & Flemings, 2000). Flow is driven from regions of high to low pressure. Far from a sand, flow in the shales is vertical. Near the sand flow is focused by the sand. Flow is captured from the shales at the base of the sand, focused along the sand, and expelled at the crest. This behavior decreases shale overpressure at the bottom of structure and increases shale overpressure at the top, while sand overpressure equilibrates to the average bounding shale overpressure.

Flow focusing has been suggested as an active process in accretionary prisms, passive margins and petroleum reservoirs. Within these studies, flow focusing has been used to explain problems in slope stability and submarine canyon formation, sea floor seeps, trap integrity and even canyon formation on Mars (e.g. Dugan & Flemings, in press; Saffer et. al, 2000; and Malin & Edgett, 2000). This thesis attempts to extend the flow focusing model by describing the hydrologic behavior in the structurally complex Bullwinkle basin in the Gulf of Mexico. I characterized and modeled flow and overpressure in 2- and 3-D to explore the effect that permeable and impermeable lens geometry has on flow focusing and the overpressure fields.

1.2. Overview

The study area is the Bullwinkle salt withdrawal mini-basin, located in blocks Green Canyon (GC) 65, 109 and 110, and a portion of the Boxer basin in GC 64 (Figures 1.1, 1.2, 1.3). This area is located at the top of the slope of the Gulf of Mexico in a water depth of 400 m (Figures 1.1, 1.2). The Bullwinkle basin is a prolific oil and gas field comprised of

three individual fields, Bullwinkle, Rocky and the J Boxer. The basin is well studied (O'Connell et al., 1996; Holman & Robertson, 1995; Kikani & Smith, 1996; Winker & Booth, 2000; Best, 2002; Comisky, 2002; Lupa et al., 2002; Swanston et al., 2002) with an abundance of data, including four 3-D seismic surveys and 70 wells. This wealth of data and interpretation make it an ideal study area. The sands that are of interest in this study are the J Sands in the Bullwinkle basin and the J Boxer sand to the west of the basin (Figure 1.3).

In Chapter 2, I presented an analyzed the effects of geometry and the flow field on sand overpressure in the Bullwinkle basin and J Sand package. Sand and shale pressure are first characterized within the basin and the implications of shallow overpressure are explored. I then described the relationship between sand pressure and the bounding shale pressure at the J Sand interval. Three numerical steady-state models were developed, a 2-D V-shaped sand, a 3-D cone shaped sand, and a 3-D cone shaped sand underlain by salt. These quantify observations around the sand, and determine the effects of sand and salt geometry on pressure in the J Sand package. Finally, I estimated sand overpressure from the surrounding shale pressure.

Chapter 3 presents an applied study of the flow focusing model. I focused on the J Boxer sand adjacent to the Bullwinkle basin in GC 64. The J Boxer is of equivalent age to the J Sand in Bullwinkle. I first described with an analytical flow model how pressures at the crests of structures are elevated due to flow focusing. Then I presented a case study of the J Boxer sand where I interpreted column height to be limited by the stress field. I closed

with a discussion of how the concept of flow focusing can be applied to assess trap integrity before drilling.

This research has addressed the role of sand geometry, impermeable strata and regional fluid flow in controlling sand overpressure. The results suggest that only a careful evaluation of these constituents will provide an accurate estimate of sand overpressure and trap integrity, and that sole consideration of the sand body is insufficient to determine the pressure and stress state of the sediments.

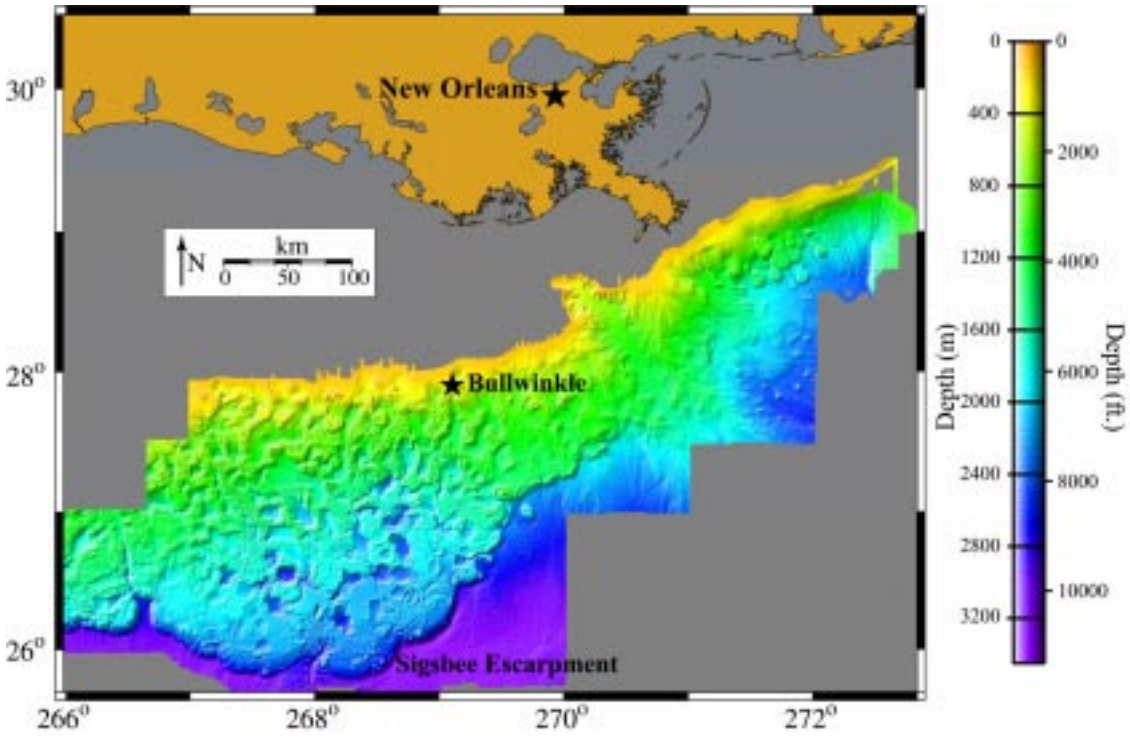

Figure 1.1: Bathymetry of the Gulf of Mexico, south of Louisiana. The location of the study area is indicated (star). The colorbar is in depth below the sea surface. Figures 1.1 and 1.2 were made using the free-ware program Generic Mapping Tool (GMT) and multi-beam bathymetry data from NOAA.

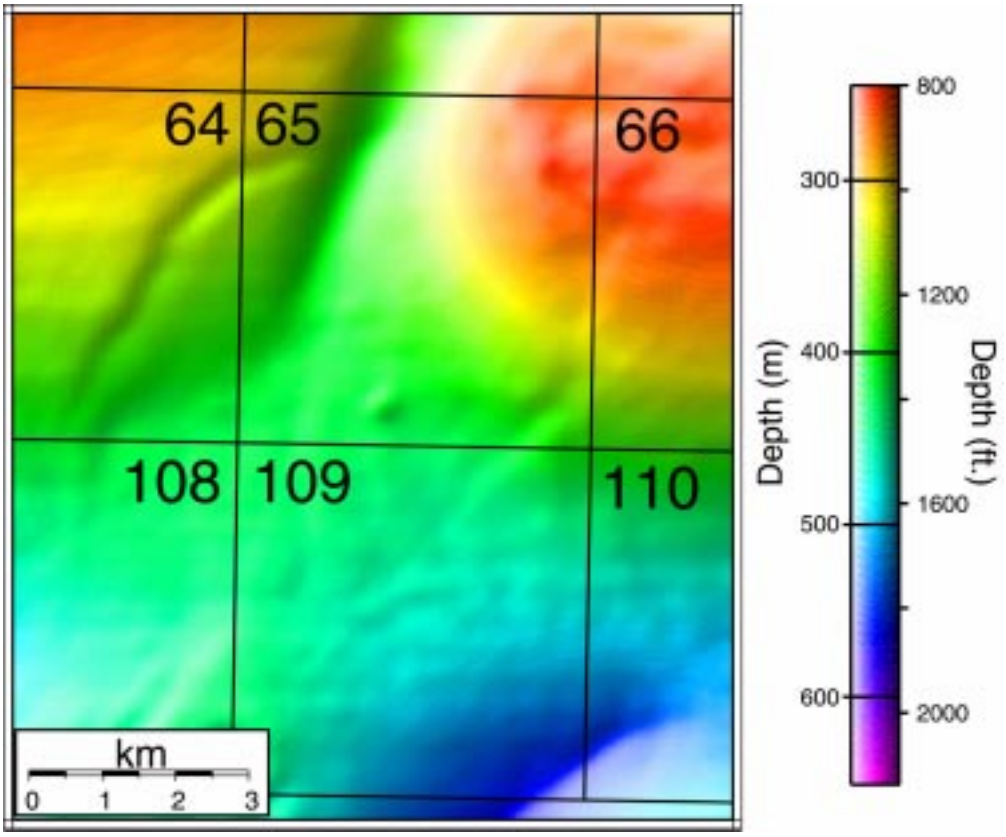

Figure 1.2: Bathymetry of the Bullwinkle basin (see Figure 1.1). The basin is located in 400 m of water. Black lines show boundaries of the OCS blocks, which are 3 miles by 3 miles. Two prominent bathymetric highs are visible to the north. The colorbar is in depth below the sea surface.

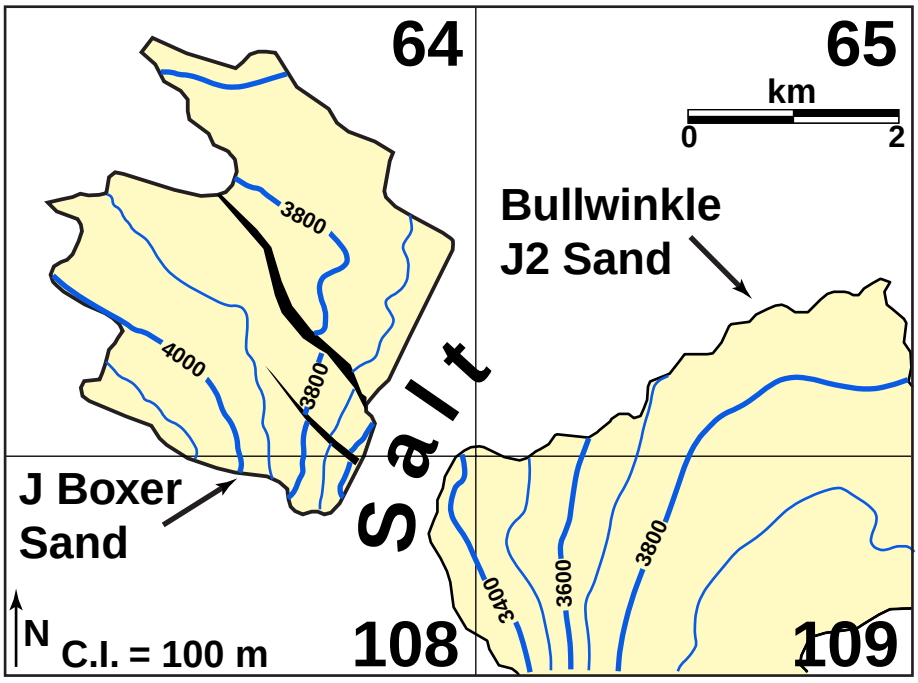

Figure 1.3: Relative locations of the two study areas. Chapter 2 focuses on the Bullwinkle basin and the J2 sand. Chapter 3 focuses on the J Boxer sand in GC 64. This sand is separated from the Bullwinkle basin by a salt high. Blue lines are structural contours in meters below the sea surface and black areas are interpreted faults.

Chapter 2: Overpressure and Flow Focusing in the Bullwinkle Field (Green Canyon 65, Gulf of Mexico)

Abstract

In the Bullwinkle mini-basin at Green Canyon 65, on the slope of the Gulf of Mexico, rapid deposition of low permeability Pleistocene sediments has generated overpressure that originates near the seafloor and increases at nearly lithostatic gradients with depth. The distribution of sand and shale pressure within the basin suggests that the flow field is influenced by structural and stratigraphic geometry. Two- and three-dimensional steady-state flow models illustrate the effects of sand and salt geometry on sand overpressure. We conclude that at Bullwinkle pressure is reduced due to an underlying low permeability salt body and the 3-D bowl-shape of the basin.

2.1. Introduction

The spatial variation of overpressure in sedimentary basins drives fluid flow and impacts the state of stress. It is critical to assess the distribution and evolution of overpressure and stress to understand the migration and entrapment of hydrocarbons and to design stable drilling programs. One method commonly used to predict fluid pressure is to relate the consolidation state of the shales to *in situ* fluid pressure. However, to correctly predict the pore pressure in reservoirs, fluid flow between shale and sand must be understood (Darby, Haszeldine, & Couples, 1998; Stump, 1998; Dugan & Flemings, 2000; Saffer, Silver, Fisher, Tobin, & Moran, 2000; and Yardley & Swarbrick, 2000).

Multiple studies have focused on the effect of high permeability lenses on flow and overpressure in basins (Traugott, 1996; Darby et al., 1998; Dugan & Flemings, 2000; Saffer et al., 2000; Yardley & Swarbrick, 2000; Lupa, Flemings & Tennant, 2002). Flow is focused through permeable beds from regions of high overpressure to regions of lower overpressure. This focusing reflects the burial history and the permeability structure of the system (e.g. Dugan & Flemings, 2000). The majority of the flow focusing research has investigated the 2-D flow field. We evaluate the effect of 3-D sand and salt geometries on the flow field and their influence on sand overpressure.

We study the Pliocene salt withdrawal mini-basin at Bullwinkle (Green Canyon 65), Gulf of Mexico (Figure 2.1). We first characterize and predict overpressure in the sand and in

the shale across the basin using *in situ* measurements and a porosity-effective stress model. We then develop 2- and 3-D, steady-state flow models that relate sand geometry to sand pressure. Finally, we model the J Sand package of the Bullwinkle basin to examine the role permeable and impermeable lenses have on the overpressure and the flow fields.

2.2. Structure and Geology of GC 65 & the J Sand Package

2.2.1. Geology of the Bullwinkle Basin

The Bullwinkle mini-basin lies 250 km to the southwest of New Orleans, Louisiana, USA (Figure 2.1), and is primarily located in blocks Green Canyon (GC) 65 and GC 109. Two oil-fields exist in the basin; Bullwinkle to the west and Rocky to the east. The basin is bounded by salt ridges to the west and southeast and by a salt diapir to the northeast (Figures 2.2, 2.3). To the northwest the basin is bounded by a normal fault that soles into the edge of salt and into the top of an evacuated salt ramp (Figure 2.3). The floor of the basin is marked by the top of salt in some areas and by a salt weld in other areas. The basin is synclinal in cross section, with major sands having up to 700 m of structural relief (Figure 2.2). In 3-D, the basin has a bowl shape (Figures 2.3, 2.4).

The Bullwinkle mini-basin formed in the Late Miocene - Early Pliocene in a complicated salt tectonic regime that transitions between the toe of a roho salt system (northwest), the toe of a stepped counter-regional salt system (eastern salt bodies) and a salt stock canopy system (southwestern salt body) (Figure 2.3) (Rowan, 1995; 1999). Salt tongues are inter-

preted to have encroached from the north, southeast and west, and to have sutured near the seafloor (Rowan, 1999). Sediment loading and gravitational collapse of the allochthonous salt formed the bowl-shaped mini-basin.

Deposits in the basin progressed from an early, sand-prone, ponded basin fill to a much shalier bypass-succession (Prather, Booth, Steffens & Craig, 1998). Prior to salt emplacement and basin formation, deposition rates were less than 1 km/Ma (Table 2.2). During basin formation, deposition rates varied from 0.24 km/Ma at 3 Ma to almost 4 km/Ma from 1 Ma to present (Figure 2.5). Faster sedimentation rates in the Late Pliocene and Pleistocene correspond to a Late Pliocene second order sea level fall and the capture of a large drainage area by the Mississippi River in the Pleistocene (Prather et al., 1998). The Late Pleistocene also represents a period of time when the Bullwinkle basin was just west of the Mississippi delta depocenter (Ostermeier, Pelletier, Winker, Nicholson, Rambow & Cowan, 2000).

2.2.2. Geology of the J Sand Package

The 3.35 Ma J Sand package is bowl-shaped with a diameter of 5 km (Figure 2.4). Although the five sands (J0, J1, J2, J3, J4) in the J Sand package are not continuous across the basin, the J2 and J0 sands together cover the extent of the basin. They range from approximately 3250 m true vertical depth beneath the sea surface (TVDSS) to nearly 4000 m TVDSS. The sands pinch out against salt to the south, east and west, and into shale to the north (Figure 2.3).

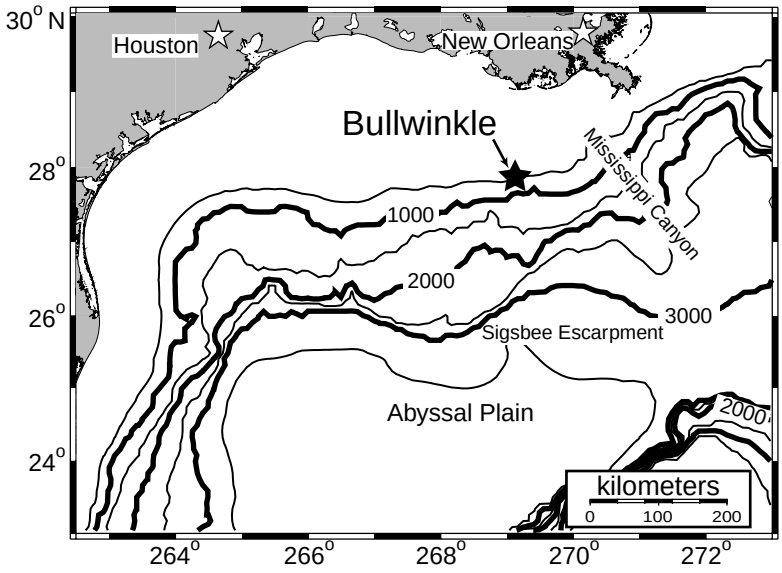

Figure 2.1: Bathymetry of the Gulf of Mexico and location of the study area. Bathymetric contours are in meters (C.I. = 500 m). The Bullwinkle basin is located in 400 m of water depth on the slope of the Gulf of Mexico in Green Canyon 65.

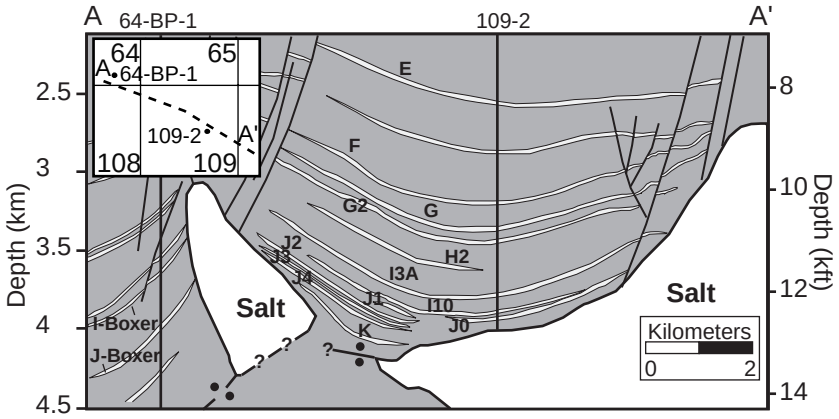

Figure 2.2: Interpreted seismic section along A-A', showing the synclinal shape of the Bullwinkle Basin. The location and orientation of the line are shown by the inset. Thick vertical black lines are the well bores of the 109-2 and 64-1-BP wells. Thin black lines are faults. Salt welds are represented by two black dots. The bottom of salt for the left salt body is not defined by seismic.

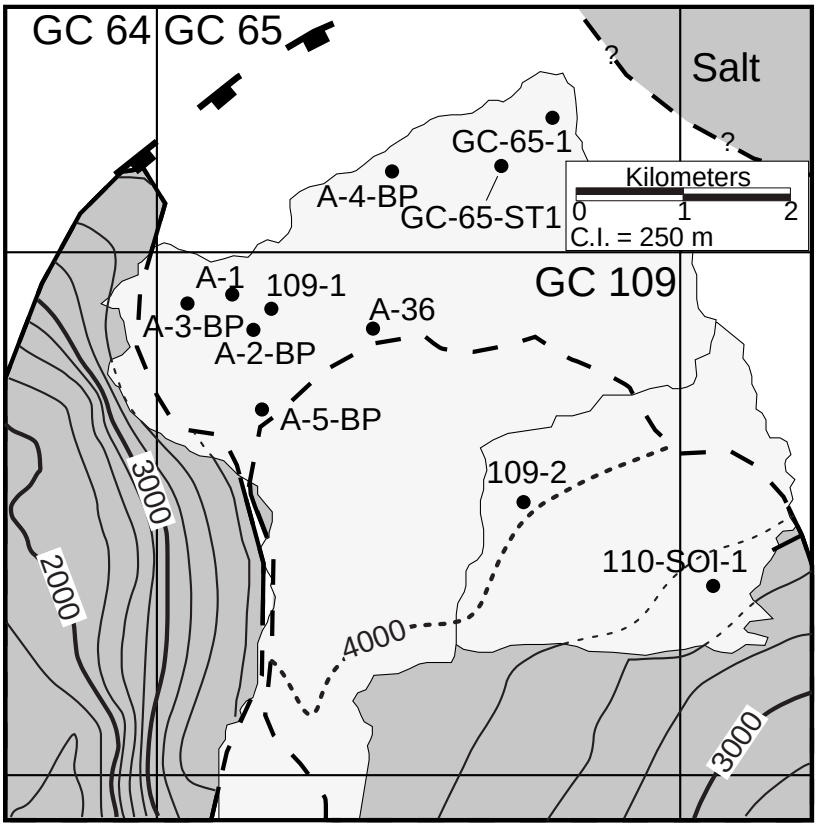

Figure 2.3:**Structure map of the top of salt in the Bullwinkle basin (dark gray) determined from 3-D seismic. Contours are in meters beneath the sea surface (TVDSS). The mapped extents of the J2 and J0 Sands are indicated with light gray (see Figure 2.4). Heavy dashed lines indicate the edge of salt beneath the J Sands. Light dashed lines are the top of salt where salt underlies the J Sand. At the 109-2 well only 100 meters separate the J Sand from the underlying salt. It is difficult to delineate the boundaries of the salt diapir to the north, however, the top lies just several hundred meters below the sea-floor.**

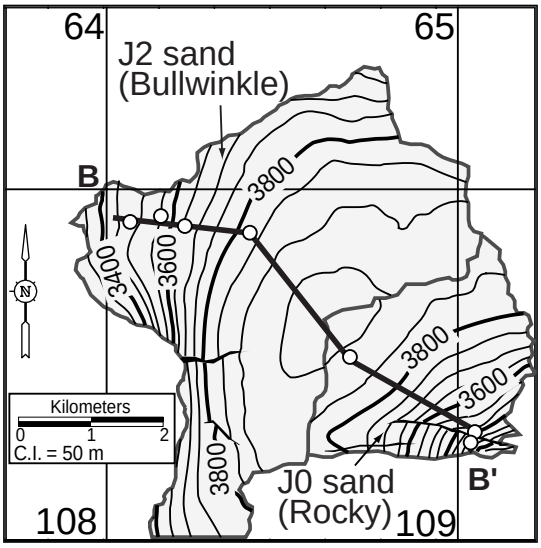

Figure 2.4: Structure map of the J-2 and J-0 sands from 3-D seismic data. The locations of wells used for transect B-B' (Figure 2.13) are indicated by white circles.

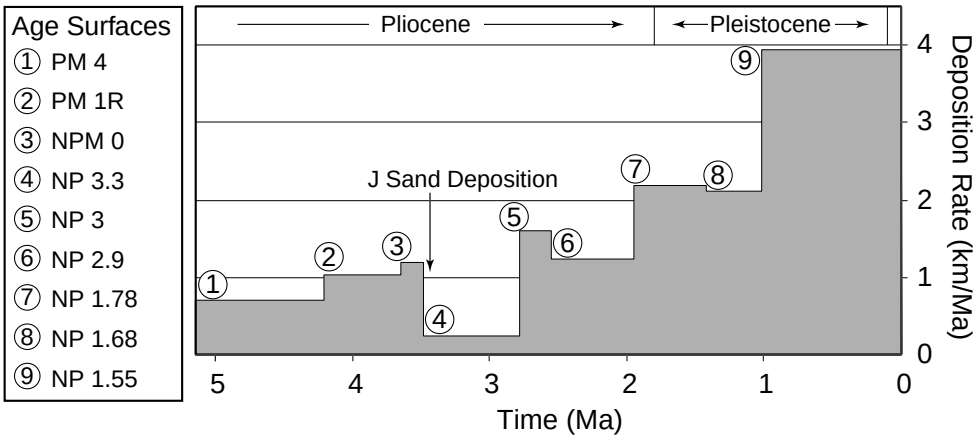

Figure 2.5: Depositional history of the Bullwinkle basin. The time periods and deposition rate are determined from well paleontological data. The stratigraphic correlation is taken from Styzen (1996) (Table 2.2).The deposition rate is found by recalculating the stratigraphic thickness at the time of deposition by assuming a surface porosity of 60%. For example a 1 km interval of sediment that was deposited over 1 Ma and has a 30% average porosity today had a deposition rate = (1 km/1 Ma) x (0.6/0.3) = 2 km/Ma.

Holman and Roberston (1994), O'Connell, Kohli and Amos (1993), and Flemings, Comisky, Liu and Lupa (2001) characterize the geology of the Bullwinkle field and the J1-J4 sands; Kikani and Smith (1996) characterize the Rocky field and the J0 sand. The J Sand package hosts the majority of the hydrocarbon reserves at GC 65 (Holman & Robertson, 1994). The sand package is bowl-shaped, and composed of interconnected channel and sheet turbidite sands that are interbedded with debris flows and shales, and are overlain by 150 m of bathyal shales. The sediments in the package coarsen upward with bedding styles that transition from ponded, internally amalgamated sands to channelized sands, indicating increasing depositional energy higher in the section (Holman & Robertson, 1994). The top of the J Sand section is characterized by multiple erosional unconformities, suggesting a period of sediment bypass in the basin (Holman & Robertson, 1994). Pressure drawdown at each well followed the same depletion curve during production (Holman & Robertson, 1994; Kikani & Smith, 1996), which indicates that all the sands are in pressure communication.

2.3. Pressure Characterization

2.3.1. Sand Pressure

Repeat formation tester (RFT) pressure measurements were taken prior to production in three wells (Tables 2.3, 2.4, 2.5) (Figure 2.6a). We assume that within the reservoirs the

fluid phases follow a hydrostatic pressure gradient, thus the water phase pressure in the reservoir is described with a single overpressure (P*).

$$P^* = P - \rho_w g z \quad , \tag{2.1}$$

where P is the fluid pressure, ρ_w is water density, g the acceleration of gravity and z is depth in TVDSS. For example, the J2 Sand has an overpressure of 19.65 MPa (Figure 2.6b).

Sand water-phase pressure ranges from 80% to over 93% of the overburden at Bullwinkle (Table 2.5) (Figure 2.6a). All sands in the basin have roughly the same overpressure (Table 2.5), with a nearly hydrostatic gradient from sand to sand. Two sands outside the basin, the I Boxer and the J Boxer (Figure 2.2), have markedly higher overpressure than the sands at equivalent depth within the basin (Figure 2.6a).

2.3.2. Shale Pressure Prediction

Shale has low permeability which precludes routine measurement of *in situ* pressure. Instead, pressure is commonly estimated from the compaction state of the shale. We used wireline data and a porosity-effective stress relation to predict shale pressure.

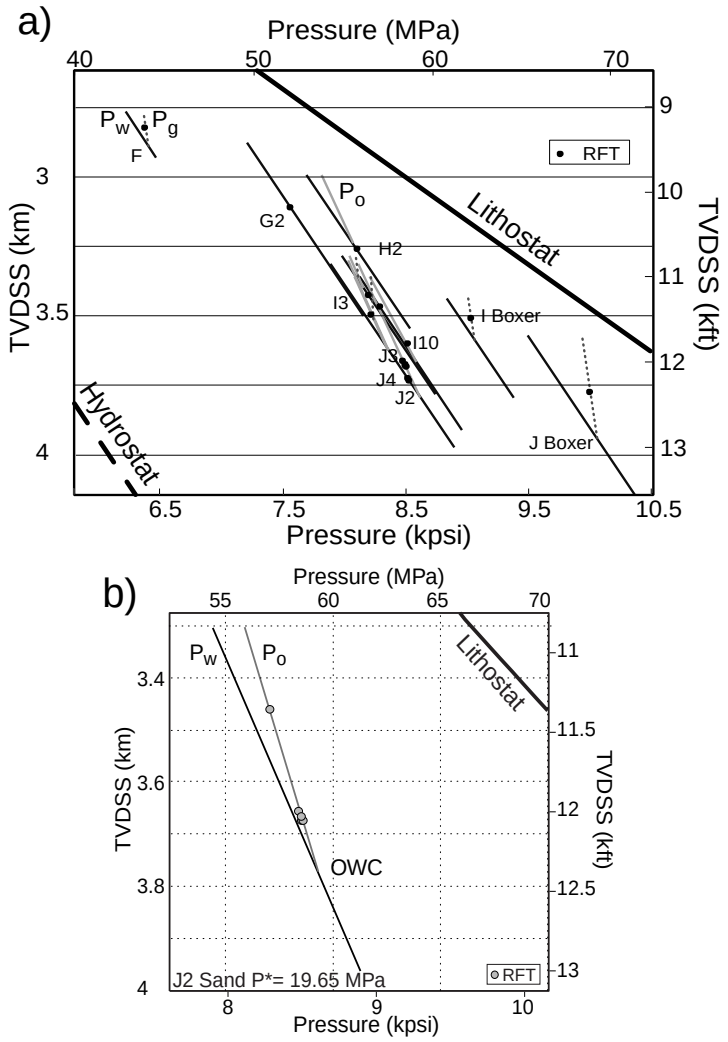

Figure 2.6: a) *In situ* pressures of the sands at GC 65. Pressures were obtained from Repeat formation tester measurements (RFTs). Water, oil and gas phase (P_w (black), P_o (grey), P_g (dotted)) pressures were calculated assuming ρ_w = 1050 kg/m^3, ρ_o = 720 kg/m^3, ρ_g = 230 kg/m^3, pressure measurements (dots), knowledge of fluid contacts from seismic, and a hydrostatic gradient. The J Boxer and I Boxer sands are located to the west of the basin (Figure 2.2). Data are referenced to true vertical depth beneath the sea surface (TVDSS). Pressure is in MPa and kilopounds per square inch (kpsi). b) Expanded view of the J2 Sand. Water phase overpressure in the J2 Sand is 19.65 MPa.

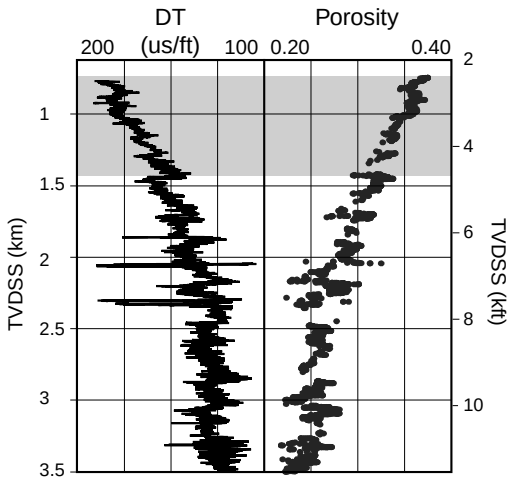

Figure 2.7: Sonic slowness (DT) in microseconds per foot (us/ft) and calculated shale porosity from Eq. (2.2) for the 109-1 well (located in Figure 2.3). The gray area shows the region that is often interpreted to be normally pressured for pressure prediction. This region is used for the Shallow Hydrostatic pressure prediction (see text).

Porosity was calculated from sonic log data using a relationship developed by Issler (1992),

$$\phi = 1 - \left(\frac{\Delta t_{ma}}{\Delta t}\right)^{\frac{1}{f}} \quad . \tag{2.2}$$

Δt_{ma} is the matrix travel-time, Δt is the sonic travel-time, and f is the acoustic formation factor. We assume f to be 2.19 for shales (Issler, 1992; Stump & Flemings, 2002). Shale pressure was predicted at each well using the empirical effective stress-porosity relationship,

$$\phi = \phi_0 e^{-\beta\sigma_v} \quad , \tag{2.3}$$

where ϕ is the porosity, ϕ_0 is the reference porosity, β is the shale compressibility and σ_v is the vertical effective stress (Rubey & Hubbert, 1959; Ham, 1966; Hart, Flemings & Deshpande, 1995). Vertical effective stress is

$$\sigma_v = S_v - P_{shale} \quad , \tag{2.4}$$

where the density log is integrated to find S_v, and P_{shale} is fluid pressure in the shale.

Two different approaches are used to constrain β and ϕ_0, the Shallow Hydrostatic approach and the Shallow Overpressure approach. For the Shallow Hydrostatic approach, a normally pressured (hydrostatic) zone was inferred between the onset of logging at 730 m TVDSS (300 meters below the seafloor (mbsf)) and 1350 m TVDSS (920 mbsf) (Figure 2.7). Shale porosity for this zone is calculated from Eq. (2.2). Lithology was filtered for clean shale by the gamma ray (GR) log; only porosity in clean shale was calculated. To

constrain effective stress, P_{shale} in Eq. (2.4) is assumed equal to the hydrostatic pressure ($\rho_w gz$). Shale compressibility and reference porosity for Eq. (2.3) are constrained with β equal to 3.62×10^{-2} MPa^{-1} and ϕ_0 equal to 40% (Figure 2.8). This approach is similar to that of Eaton (1975) and Hart et al. (1995).

In the Shallow Overpressure approach, we use RFT measurements to constrain the porosity-effective stress model (Eq. (2.3)) (Figure 2.6a). Effective stress for the shale overlying an RFT measurement is calculated from Eq. (2.4), where P_{shale} is assumed to be equivalent to the sand RFT (Table 2.5). Shale porosity at the sand top is estimated by projecting calculated shale porosity to the sand-shale interface (Table 2.6:). Error bars in Figure 2.8 correspond to the water phase effective stress at the top and bottom of structure. With this approach, the shale compressibility is found to equal 3.92×10^{-2} MPa^{-1} with a reference porosity of 37.5% (Figure 2.8).

The two approaches produce different porosity-effective stress behaviors (Figure 2.8). The most striking difference is that the effective stress predicted by the Shallow Hydrostatic approach at the base of the hydrostatic section (at 920 mbsf) is equal to the effective stress predicted with the Shallow Overpressure approach in the J Boxer sand (3360 mbsf) (Figures 2.2, 2.8). However, the shales at the J Boxer are more compacted (28% vs. 32% porosity). This either means that the β determined in the shallow section does not apply for the deeper sediments (cf. Hart et al.,1995) or that the assumption of hydrostatic conditions for 0-920 mbsf (the Shallow Hydrostatic approach) is incorrect.

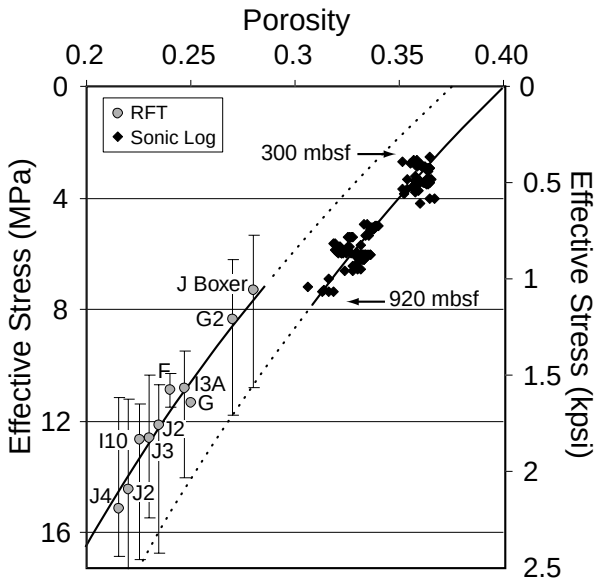

Figure 2.8: Relationship of shale porosity (from DT; black diamonds) to shale vertical effective stress. Vertical effective stress for the Shallow Hydrostatic approach (sonic log) is determined assuming that the shale is normally pressured from 300-920 meters below the seafloor (mbsf). Shale effective stress for the Shallow Overpressure approach is calculated from the RFT measurements (gray circles), assuming shale overpressure is equal to adjacent sand overpressure. The error bars represent water phase effective stress at top and bottom of the sand. Regressions of Eq. (2.3) yield $\beta = 3.62 \times 10^{-2}$ MPa^{-1} and $\phi_0 = 40\%$ for the Shallow Hydrostatic approach, compared to 3.92×10^{-2} MPa^{-1} and 37.5% for the Shallow Overpressure approach.

Shale pressure is calculated by rearranging Eq. (2.3),

$$P_{shale} = S_v - \left(\frac{1}{\beta}\right)\ln\left(\frac{\phi_0}{\phi}\right) \quad . \tag{2.5}$$

Shale pressure predicted from the Shallow Hydrostatic approach is lower than measured sand pressure (Figure 2.9). For example, the pressure mismatch between the predicted shale pressure and the measured pressure in the F Sand is ~4 MPa (Figure 2.9). The shale pressures predicted by the Shallow Overpressure approach match those observed in the sands (Figure 2.9). The Shallow Overpressure approach also predicts that overpressure in the Bullwinkle basin begins at a very shallow level, reaching a magnitude of 2.5 MPa at just 600 mbsf ($P \sim 0.8\ S_v$) (Figure 2.10).

We interpret that the Shallow Overpressure approach is correct. Shallow overpressure is common in areas where the sedimentation rate is high (Dugan & Flemings, 2000; Ostermeier et al., 2000). Ostermeier et al. (2000) measured overpressure in the mud at the seafloor at Mississippi Canyon 810 (300 km from GC 65; 1100 m of water), which is a region with a similar Pleistocene to Recent depositional history. Shale is overpressured at the seafloor and overpressure reaches 2.75 MPa at 600 mbsf ($P \sim 0.8\ S_v$). Modeling also predicts that deposition rates of 4 km/Ma of low permeability clay and silt will generate significant overpressure (Gibson, 1958; Gordon & Flemings, 1998; Dugan & Flemings, 2000).

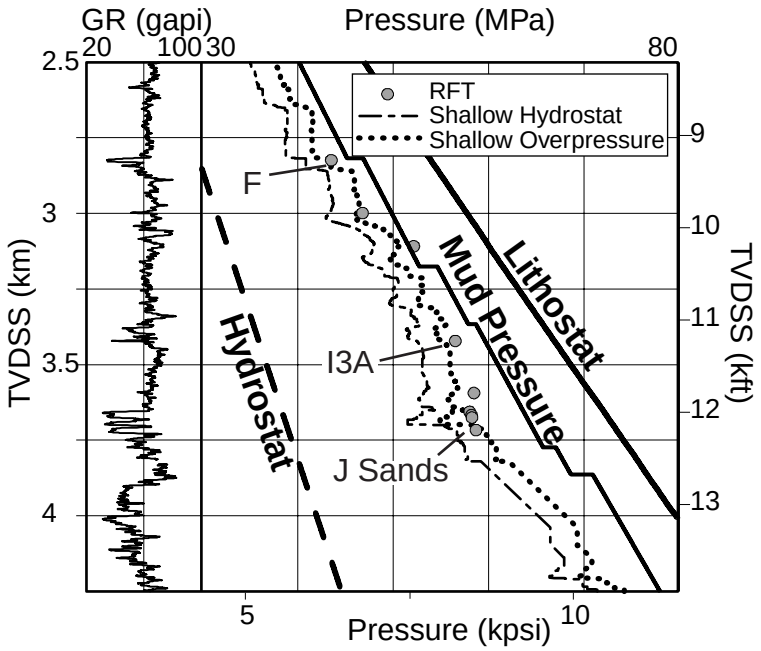

Figure 2.9: Comparison of predicted shale pressures from the sonic log of the 109-1 well to RFT water phase pressures taken in the 109-1 well. The Shallow Hydrostatic approach (thin dashed line) predicts shale pressure much lower than observed water phase sand pressure. The Shallow Overpressure approach (dotted line) is constrained on the observed values.

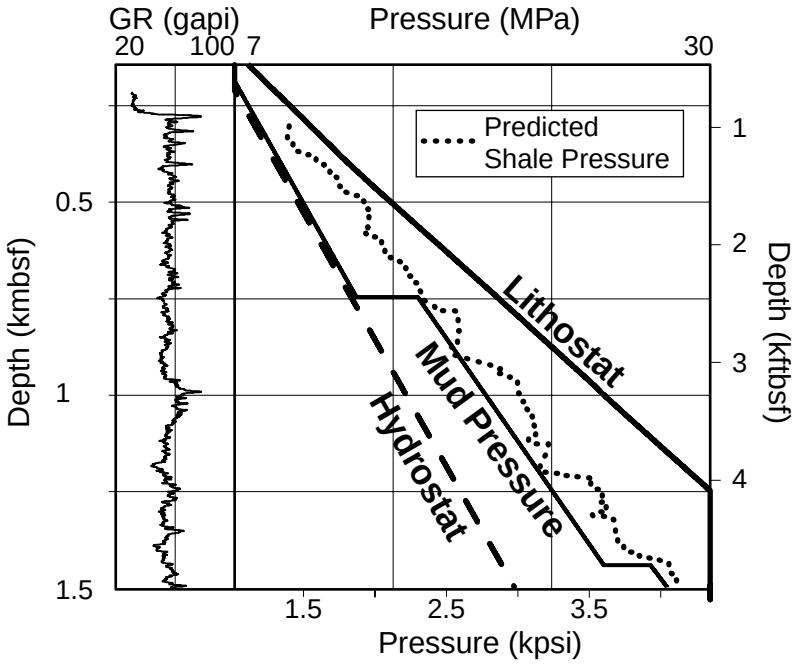

Figure 2.10: Predicted pressure in the shallow section of the 109-1 well from the Shallow Overpressure approach. The data are referenced in kilometers below the seafloor (kmbsf). The dotted line is predicted shale pressure and the solid line is the mud pressure used for drilling the 109-1 well. Based upon the effective stress - porosity behavior deep in the basin, we interpret that the shallow section is overpressured starting near the seafloor.

2.3.3. Pressure in the J Sand Package

We predict a spatial variation in the overpressure field surrounding the J Sand based upon the compaction state of the bounding shale. Shale overpressure at the sand-shale interface is often difficult to predict because sand content gradually increases near the clean sand, thus clean shales are not sampled and pressure is not predicted. In addition, a sharp variation often occurs in the compaction state of the shale as the sand is approached (e.g. Figure 2.11c). To estimate the shale overpressure at the sand-shale interface we linearly extrapolate calculated shale overpressure to the sand top (Figure 2.11).

We find that near the top of structure (wells A-3-BP, 110-SOI1, A-1) shale overpressure increases linearly into the sand (e.g. Figure 2.11a). Shale overpressure in these wells is lower than sand pressure at the sand-shale interface. At the bottom of structure, shale pressure in most wells decreases into the sand at a short wavelength (wells A-4-BP, A-5-BP, GC-65-1 and GC-65-1-ST) (Figure 2.11). In these wells, the extrapolated shale overpressure is higher than sand overpressure.

Everywhere shale is penetrated by a well, porosity is approximately constant above the sand. This results in a predicted lithostatic shale pressure gradient with depth along the top of the sand (Figure 2.12). Wells that overly the salt tend to fall below the trend (e.g. wells

A-36, 109-2). The different pressure gradients in the sand and the shale lead to higher shale pressure than adjacent sand pressure at the bottom of the structure and higher sand pressure than shale pressure at the top of the structure (Figure 2.12). At a depth of 3575 m TVDSS, shale pressure and sand pressure are equal.

A shale overpressure cross-section is constructed from six wells in the basin (Figure 2.13). Similar to Figure 2.12, at top of structure, bounding shale overpressure is less than sand overpressure, while at base of structure it is higher than sand overpressure (Figure 2.13). The shale overpressure gradient above the limbs (10.5 MPa/km) is higher than that above the center of the sand (7.0 MPa/km). Beneath the J Sand at the 109-1 well, which lies between the two salt bodies, the overpressure gradient is greatest (~20 MPa/km).

The relationship between a dipping permeable sand and a less permeable bounding shale has been well-studied (e.g. Traugott, 1996; Stump & Flemings, 2000; Yardley & Swarbrick, 2000; Lupa et al., 2002). The overpressure behavior in this system has been attributed to a combination of loading geometry and flow focusing through the sand. The permeable sand focuses fluid from low on structure to high on structure. This elevates pressure high on structure and diminishes it low on structure. We developed steady-state flow models of the J Sand to explore this behavior.

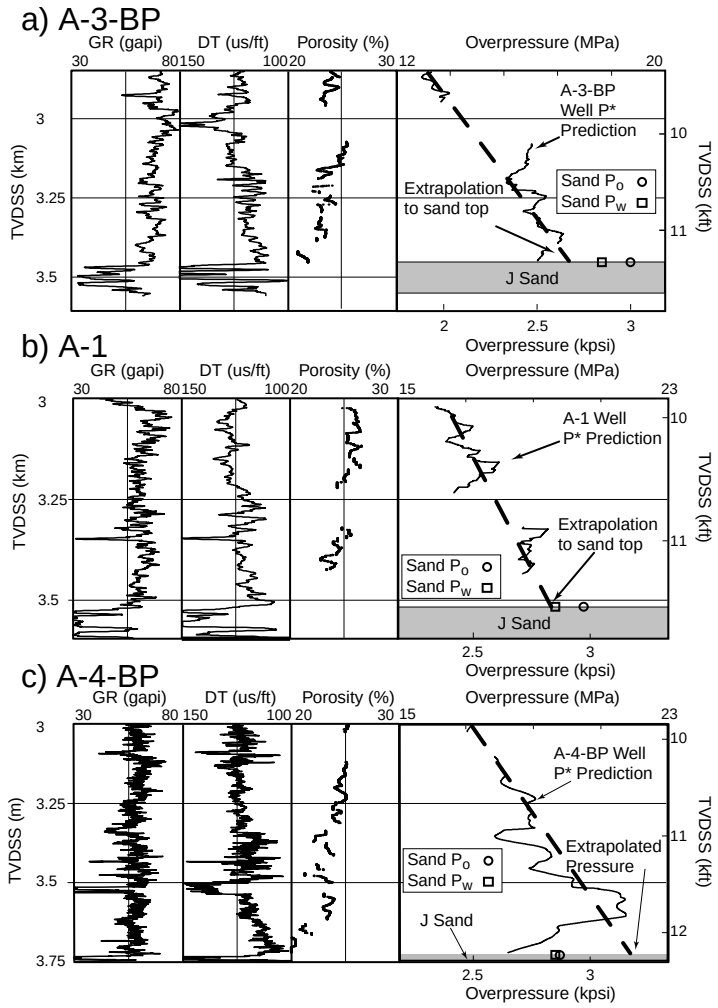

Figure 2.11: Predicted shale overpressure at a) the A-3-BP well; b) the A-1 well; and c) the A-4-BP. When the sonic log does not extend to the sand top, shale overpressure is projected to the sand top (dashed line). The projected shale overpressures are used for Figure 2.12. Measured water phase (square) and oil phase (circle) overpressures for the J1 sand are indicated at the sand-shale boundary. The gamma ray log (GR), sonic log (DT) and calculated shale porosity are shown for reference.

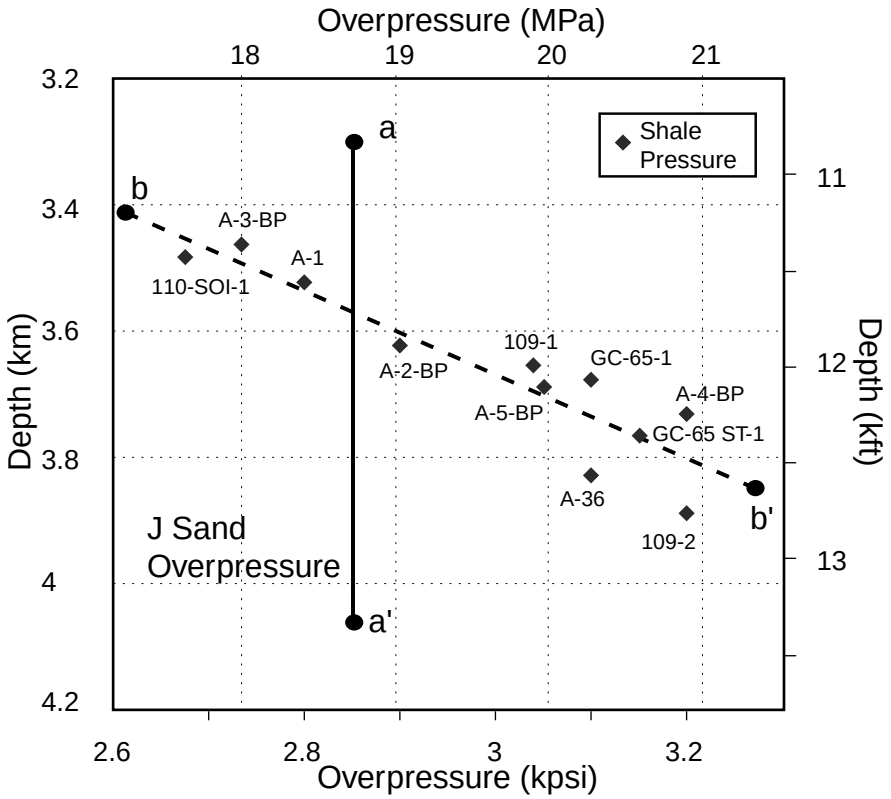

Figure 2.12: Predicted shale overpressure above the J-Sand (black diamonds) and water phase overpressure of the J Sands. The predicted shale overpressure gradient is 9.6 MPa/km. The 110-SOI-1, 109-2 and A-36 wells overlie salt. The penetrations are located in Figure 2.3. The overpressure trends a-a' and b-b' are shown in later figures.

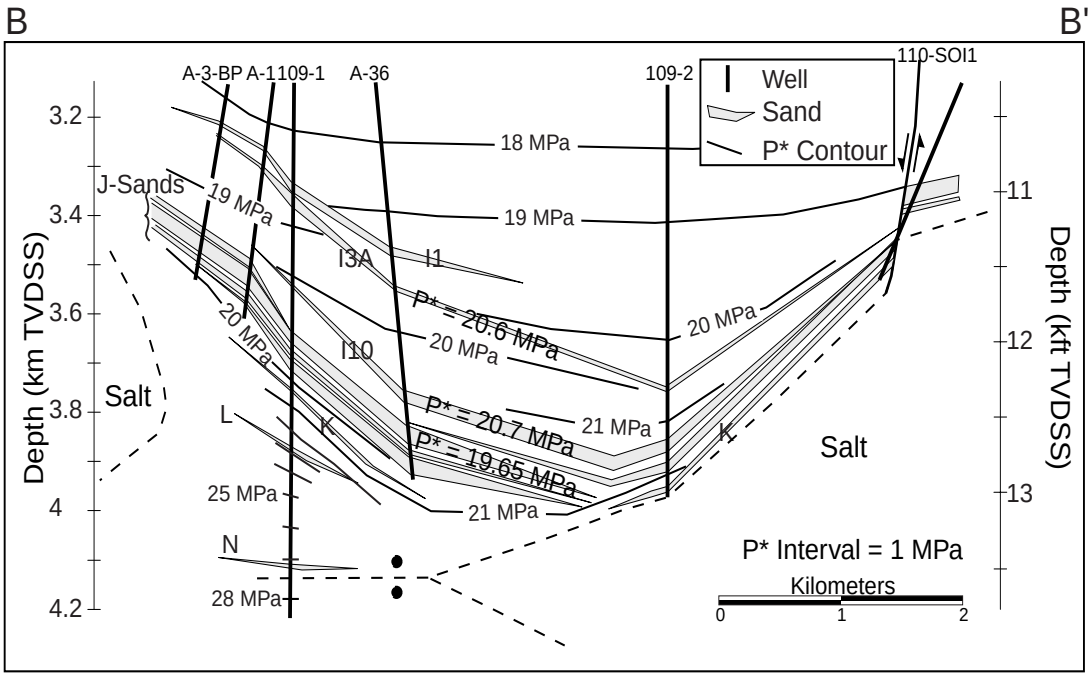

Figure 2.13: Overpressure cross-section through the Bullwinkle field along B-B' (located in Figure 2.4). Wells bores are indicated by vertical black lines. The overpressure contours are extrapolated from well to well. Sand overpressure is from RFT measurements. Salt bodies are shown with dashed lines, with salt welds indicated by black dots. The shale overpressure surrounding the sand is higher at bottom of structure and lower at top. Different shale overpressure gradients exist along structure between 2900 m TVDSS and the sand top, ranging from 10.5 MPa/km at the A-3-BP to 7 MPa/km at the 109-2. A very high overpressure gradient exists beneath the sand at the 109-1 well, ~ 20 MPa/km. The shallower I3A and I10 sands are at a higher overpressure than the deeper J Sands.

2.4. Model

A steady-state, finite-difference flow model was developed to simulate flow and overpressure in the Bullwinkle basin. The model solves the diffusion equation in either 2-D cartesian or 3-D radial coordinates (Appendix A) (Figure 2.14). Vertical shale permeability of $1x10^{-21}$ m^2, horizontal shale permeability of $1x10^{-19}$ m^2, isotropic sand permeability of $1x10^{-12}$ m^2 and an isotropic salt permeability of $1x10^{-23}$ m^2 were assumed (Neuzil, 1994; Stump, 1998; Best, 2002).

Three models were developed: (1) a 2-D V-shaped sand (2-D Model), (2) a 3-D cone-shaped sand (3-D No Salt Model) and (3) a 3-D cone-shaped sand with an underlying salt body (3-D Salt Model) (Figure 2.14). For all models shale overpressure was set to 14.52 MPa at 3020 m depth and 30.16 MPa at 4670 m depth, which set the far-field shale overpressure gradient to 9.6 MPa/km. The structural low of the modeled sand was placed at 3640 m depth, equivalent to the bottom of the J Sand package. The structural high of the sand, at 4050 m depth, was calculated by setting the average depth of the 3-D cone-shaped sand equal to the average depth of the J Sands (Table 2.7). The tops of some of the members of the J Sand package are higher, but the sands are not continuous around the basin at shallower depths (Figure 2.4).

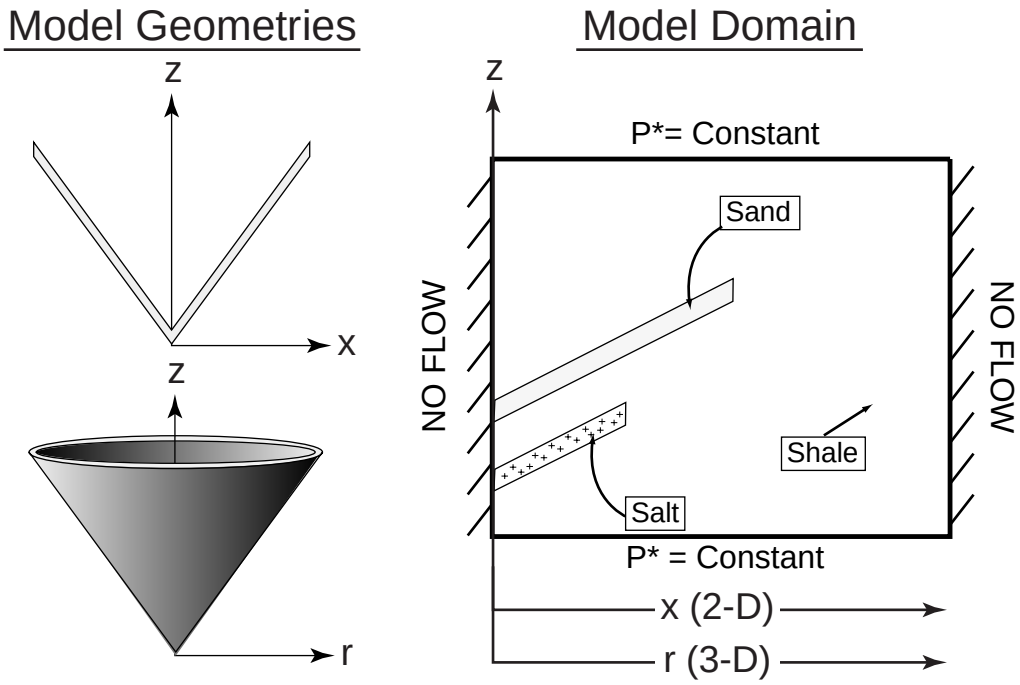

Figure 2.14: A synclinal shaped basin is modeled in 2-D as a V-shape and in 3-D as a cone. Because of the symmetry of the modeled geometries, no flow occurs across the center of the basin. Thus, the model domain needs to encompass only one limb of the sand. The top and bottom boundary conditions are constant pressure boundaries. The side boundaries are no flow. The sand and salt bodies are placed against the left boundary, which represents the center of the basin.

In the 2-D Model, sand overpressure is a constant 21.7 MPa (Figure 2.15). In the shale, overpressure contours are sub-parallel to sand structure (Figure 2.15a). The overpressure in the bounding shale is equal to sand overpressure everywhere on structure. At the top of the structure, shale overpressure is elevated with respect to the far-field shale overpressure. At the bottom of the structure, in the cusp or 'V' of the sand, shale overpressure is depressed with respect to the far-field shale overpressure (Figure 2.15b). Above the sand, the vertical shale overpressure gradient is highest at the top of structure and decreases toward the middle of the sand (Figure 2.15a, b). Beneath the sand, the vertical shale overpressure gradient is highest in the middle and decreases outward. A vertical well penetrating the apex of the sand would encounter a high shale overpressure gradient above the sand (16.5 MPa/km), followed by a lower gradient beneath the sand (2.4 MPa/km) (Figure 2.15b). A well penetrating the structural low of the sand would encounter a shale overpressure gradient of 1.6 MPa/km above the sand, and a much higher gradient (20.5 MPa/km) beneath the sand (Figure 2.15b).

The high overpressure gradient from low to high on structure drive flow focusing through the sand. Flow is driven from regions of high overpressure to regions of low overpressure (Figure 2.15a). Far from the sand flow is vertical, but near the high permeability sand the flow field is perturbed. Streamlines converge into the base of the sand and diverge from the top; this process records the capture of fluid at the base of structure, focusing of fluid along the sand, and expulsion of fluid at the apex. Minimal flow occurs in the shale above the cusp of the sand because the sand has diverted the majority of the fluids upstructure.

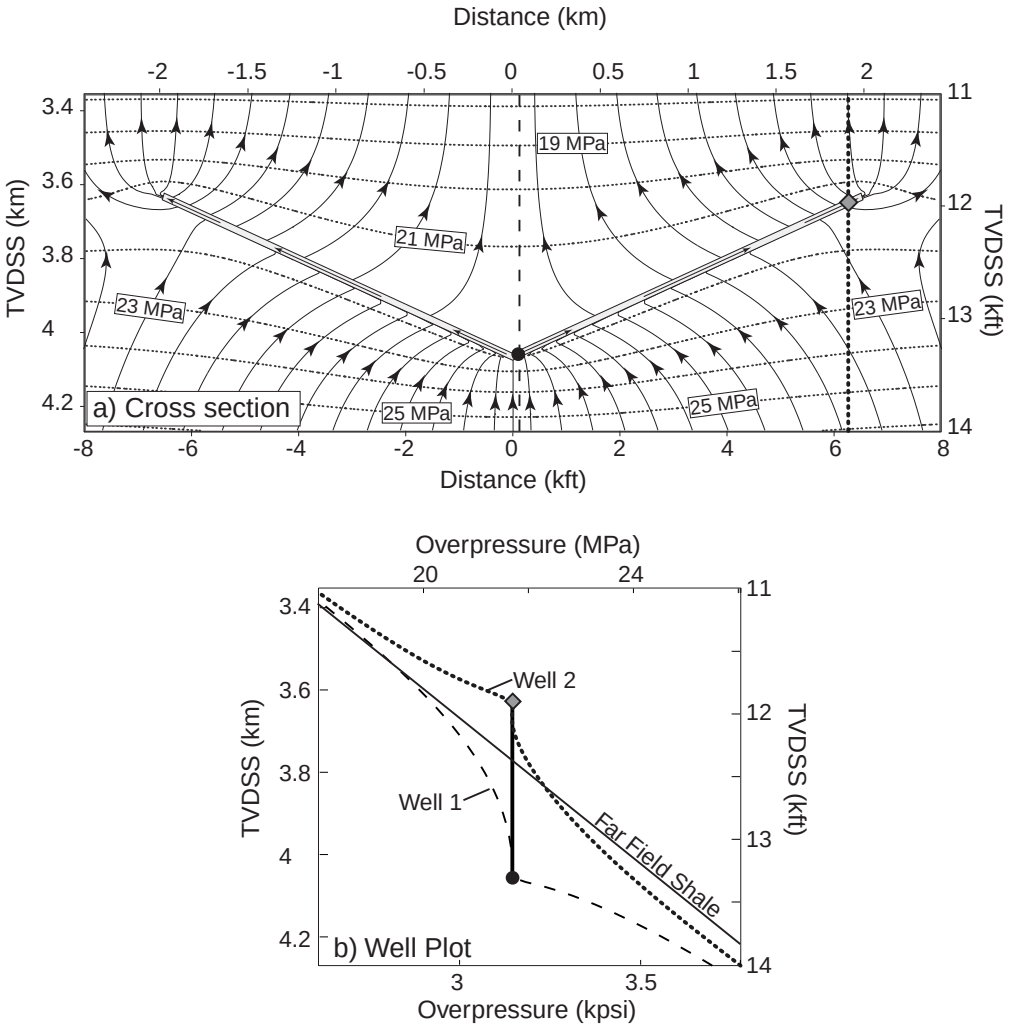

Figure 2.15: a) Overpressure and flow in the 2-D Model. The thin dotted black lines are overpressure contours. The vertical black lines with arrows are streamlines. Flow occurs along streamlines, and fluid flux between adjacent streamlines is constant. Where streamlines are close together, fluid velocity is fast; where they are far apart, fluid velocity is slow. The arrows within the sand (light gray) are schematic. b) Overpressure profiles for vertical wells drilled through the bottom of structure (Well 1 - dashed line), and the top of structure (Well 2 - dotted line). The thick vertical line is the sand overpressure. The far field shale overpressure is shown for reference (solid line). Well locations are shown at the top of Figure 2.15a.

The flow behavior in the shale corresponds to the overpressure field; where shale overpressure gradients are high, higher fluid flow occurs; where shale overpressure gradients are low, little flow occurs (Figure 2.15a).

The 3-D No Salt model predicts a similar overpressure behavior to the 2-D Model (Figures 2.16a, b). The sand overpressure is constant (21.1 MPa), which is 0.6 MPa lower than predicted in the 2-D Model. A well drilled at the apex of the sand would encounter a shale overpressure gradient of 13.8 MPa/km above the sand. At the bottom of structure, above the cusp of the sand, the modeled shale overpressure gradient is 1.1 MPa/km, whereas beneath the cusp, the modeled shale overpressure gradient is 25.1 MPa/km (Figure 2.16b).

The addition of a very low permeability salt beneath the sand disturbs the regional overpressure field. Sand overpressure in the 3-D Salt Model is 0.6 MPa lower than predicted by the 3-D No Salt Model (20.5 MPa) (Figure 2.16c). Above the sand, the overpressure gradients are lower relative to the 3-D No Salt Model, 11.9 MPa/km at the top of structure and 1.0 MPa/km above the cusp. At the edge of salt, the overpressure gradient (21.4 MPa/km) significantly exceeds the far-field gradient (9.6 MPa/km). A vertical well penetrating the cusp of the sand and salt would record an overpressure jump in excess of 5 MPa across the salt body (Figure 2.16c).

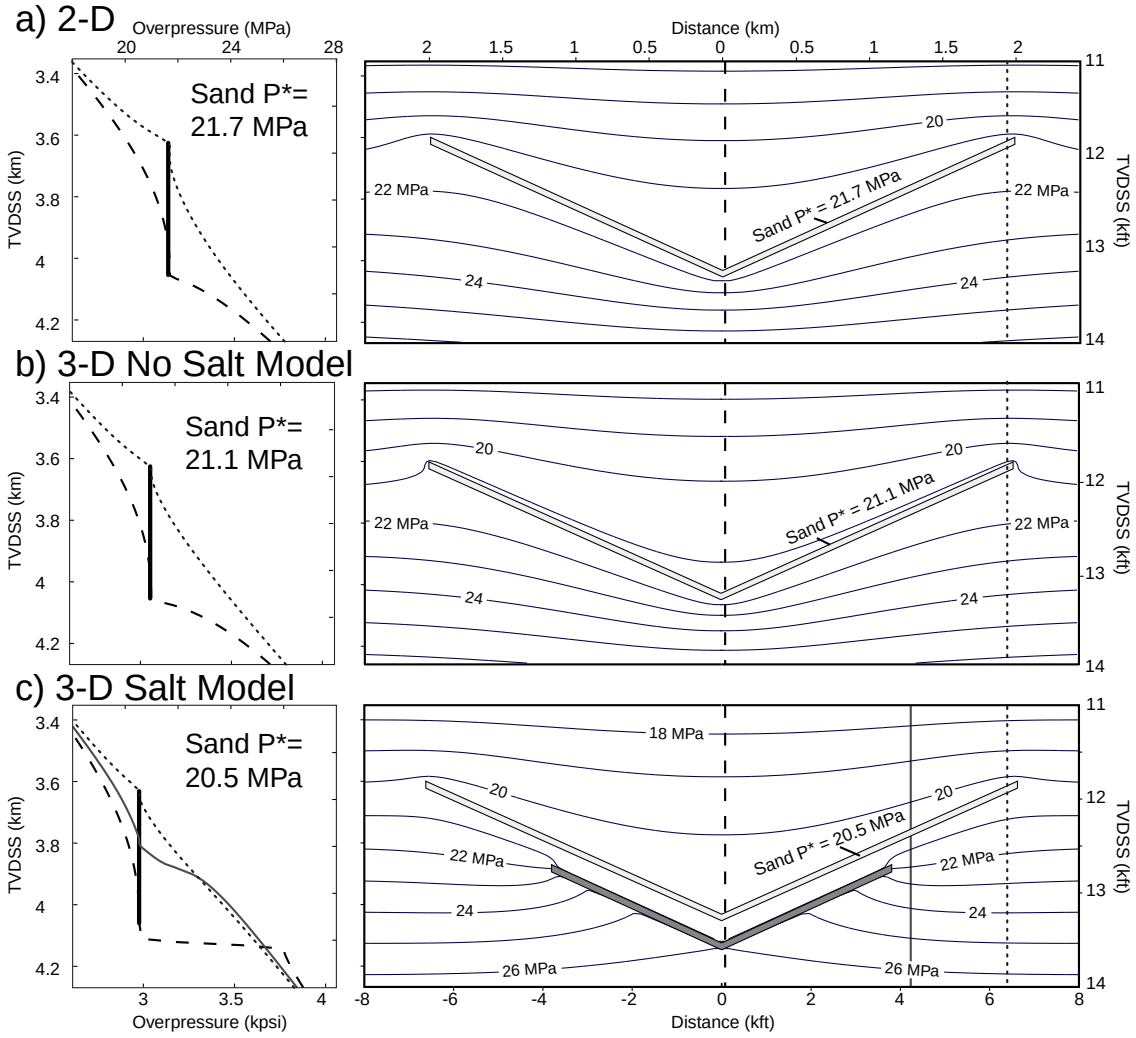

Figure 2.16: Overpressure predicted in a permeable sand and surrounding shale based on three geologic models: a) a 2-D V-shaped sand (light gray); b) 3-D No Salt Model of a cone shaped sand; c) 3-D Salt Model of a cone-shaped sand underlain by a salt body (dark gray). Plots on the left are overpressure in wells drilled at the top of structure (dotted line), middle of structure (dashed line) and just off the edge of salt (Model (c) solid line).

In our models, overpressure and flow are controlled by the far-field overpressure gradient and the permeability architecture (e.g. Stump & Flemings, 2000; Yardley & Swarbrick, 2000; Lupa et al., 2002). We impose a constant far-field gradient, therefore differences in the permeability structure of the models dictate the different sand and shale overpressures.

Flemings, Stump, Finkbeiner, and Zoback (in press) define how undrained systems have sand overpressure equal to the average of the bounding shale overpressure. Lupa et al. (2002) showed that simple, linear geometries at steady-state flow conditions also have this behavior. We show that this is approximately the case for an isolated sand, whether V-shaped or cone-shaped (Figure 2.17); however, the method breaks down when a salt layer is present.

A larger percentage of the 3-D sand is shallower than the 2-D sand because of its cone-shaped geometry (Figure 2.17). The average depth of a 3-D cone-shaped sand lies 1/3 of the way down from top of structure (3777 m depth in our model), while the average depth of a 2-D sand is at the midpoint (3845 m depth in our model) (Figure 2.17). This difference in geometry lowers sand overpressure 0.65 MPa in the 3-D model (Figure 2.17). Sand and far-field shale overpressure are approximately equal at the average depth for the 2-D Model and the 3-D No Salt Model. They are not equal at exactly the average depth because the shale in the cusp of the sand is isolated and is unable to recharge after draining into the sand. At steady-state, this lowers the average bounding shale overpressure and lowers sand overpressure.

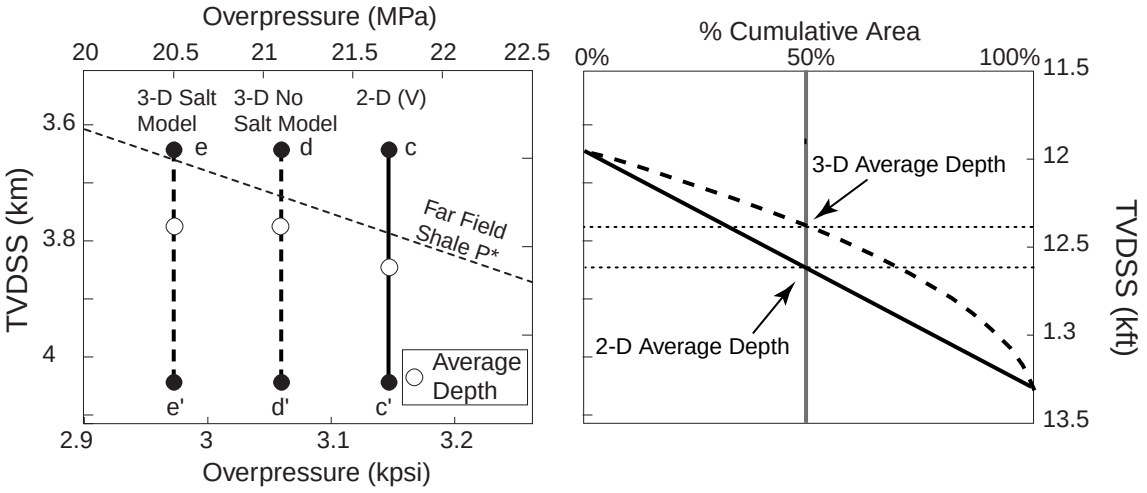

Figure 2.17: Comparison of the sand overpressure and geometry of the three models. On the left is a overpressure-depth plot illustrating the relationship of sand overpressure to the far-field gradient (thin dashed line) and the average sand depth (white circles). On the right, the cumulative percentage of area is plotted against depth. The 2-D sand (solid line) has half of its area above the midpoint and half below, thus the average depth (50% cumulative area) is at the midpoint. The 3-D cone shaped sand has more area above the midpoint than below, resulting in an average depth 1/3 of the way down from top of structure.

In the 3-D Salt Model, the effect of sand geometry is overshadowed by the effect of the very low permeability salt layer. Between the sand and the salt, no overpressure gradient exists. No flow occurs into the sand where it is underlain by salt. Directly beneath the center of the salt body, the shale overpressure gradient is ~3 MPa/km and little flow occurs. The very high shale overpressure gradient at the edge of the salt dictates a high fluid velocity around the edges of the salt body. As fluids migrate upward, the low permeability salt deflects fluids laterally, and shields the sand from receiving flow from the underlying higher overpressured shale (Figure 2.16c). This decreases the overpressure of the bounding shale and reduces sand overpressure (Figure 2.17). The flow focusing effect is also diminished, as the sand only receives fluid flow above the top of salt (~3800 m depth). Less fluid is focused upstructure and expelled at the crest, decreasing the shale overpressure gradient at the top of structure (Figures 2.16c).

2.5. Discussion

Model results predict that sediments above a salt body have a lower overpressure and a lower overpressure gradient than those that are not underlain by salt (Figure 2.16). This is supported in the Bullwinkle basin where sand overpressure is lower than it is at an equivalent depth outside the basin (Figure 2.6a). Overpressure from sand to sand follows a lower gradient inside the basin than outside. The salt (Figure 2.3) partially shields the overlying sediments above, resulting in the lower overpressure inside the basin relative to outside. This suggests that at a regional scale, very low permeability layers control overpressure. Basins that overly salt will have lower pressures than similar basins not overlying salt.

In our models, a high shale overpressure gradient is observed above the sand crest, with a lower shale overpressure gradient in the center (Figure 2.16). The Bullwinkle well data has a similar behavior. For example, the overpressure gradient at the A-3-BP well is 1.5 times greater than deeper in the 109-2 well (Figure 2.13). Therefore, we interpret that the J Sand is capturing flow at the center, focusing flow laterally upstructure, and expelling fluids at the crest.

The underlying salt also modifies the flow and overpressure behavior around the sand. The 3-D Salt Model predicts an amplified shale overpressure gradient (21.4 MPa/km) at the edge of a salt body (Figure 2.16). At the 109-1 well, which is located off the edge of two salt tongues (Figure 2.3), the shale overpressure gradient beneath the sand is 20 MPa/km (Figure 2.13). The 3-D No Salt Model predicts a much lower gradient (~10 MPa/km) for the same location. This suggests salt shields the majority of the sand from fluid flow, diverts fluids laterally and elevates overpressure between the salt bodies at the 109-1 well.

In the modeled well profiles, overpressure is continuous from the shale into the sand (Figure 2.16). Porosity-based predictions, however, suggest an abrupt overpressure jump is present at the J Sand-shale interface (Figure 2.11a). The mismatch above the depth where sand and shale overpressure are equal (~3575 m) may be due to unloading (Yardley & Swarbrick, 2000; Flemings et al., in press). Flow focusing elevates pressure at the top of structure, which decreases effective stress. Porosity loss due to compaction is irreversible, so there is no corresponding porosity increase during unloading. If unloading has

occurred, our effective stress-porosity model under-predicts pore pressure (e.g. Bowers, 1994).

Below 3575 m TVDSS careful examination shows that sand and shale pressure may be equal at the sand-shale interface. The mismatch between overpressure predicted by the well data and known sand overpressure is because near the sand, shale pressure changes rapidly in the vertical direction (Figures 2.11c, 2.15b). Shale overpressure at the sand-shale interface is estimated over a large vertical depth range, which does not capture the rapid variation in shale overpressure and results in an overestimate of the bounding shale overpressure (e.g. Figure 2.11c). The large vertical overpressure gradient near the sand is an effect of anisotropy in the shale. Horizontal shale permeability is greater than the vertical shale permeability, so shale preferentially drains horizontally rather than vertically. Thus, far from the sand in the vertical direction, shale overpressure does not reflect sand overpressure. Alternatively, the mismatch may indicate that the shales are still draining and that the overpressure and flow fields are still evolving.

To ascertain the implications flow focusing and flow shielding have for sand pressure prediction, we predicted J Sand pressure from its geometry and the surrounding shale pressure (i.e. independent of flow) and compared our prediction to measured J Sand pressure. All five hydraulically connected sands in the Bullwinkle basin (J0-J4) were used to estimate sand overpressure (Table 2.7).

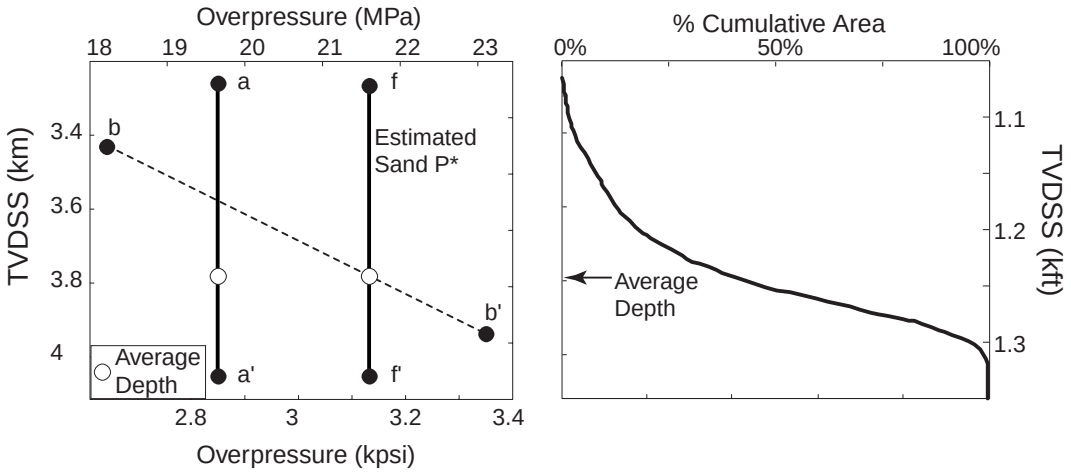

Figure 2.18: Discrepancy between the J Sand overpressure measured by RFT measurements (a-a') and that estimated from the bounding shale overpressure and sand geometry (f-f'). The J Sands have an average depth of 3785 m TVDSS (Table 2.7). Sand overpressure is overestimated by 2 MPa when we assume shale overpressure and sand overpressure are equal at the average depth. Observed sand overpressure and far-field shale pressure are from Figure 2.12.

Average depth for the J-sand package in Bullwinkle is 3785 m TVDSS (Figure 2.18). Sand pressure is assumed to equal the bounding shale pressure at the average depth (Figure 2.18). Estimated sand overpressure from geometry (Flemings et al., in press) is 21.6 MPa, almost 2 MPa greater than measured water phase overpressure in the J Sands (19.65 MPa). This is similar to the 3-D Salt Model, where sand overpressure would be overpredicted by

1.2 MPa if the far field shale pressure and sand geometry are used to predict sand pressure (Figure 2.17). This implies that in a complex geological setting, stratigraphic geometry alone is not sufficient to characterize sand overpressure and that the effect of the flow field and impermeable lenses must be considered.

2.6. Conclusions

The distribution of sand and shale overpressure within the Bullwinkle basin suggests that overpressure and fluid flow are controlled by structural and stratigraphic geometry. The flow focusing model applies, but the 3-D sand geometry and the underlying low permeability salt modify overpressure and fluid flow. Around the J Sand package, overpressure is controlled by the flow behavior between the high permeability sand and the surrounding lower permeability sediments. The underlying salt reduces fluid flow and pressure source to the J Sand, so the overpressure in the J Sand package is lower than geometric analyses predict. Additionally, the shallower depth distribution of the 3-D bowl-shaped sands results in a lower sand overpressure as the sands are dominantly charged by lower overpressured shale.

Dynamic predictions of overpressure from fluid flow modeling provide insight into the petrophysical behavior of the sediments in the Bullwinkle basin. Simple, steady-state models illuminate the fluid flow processes that control porosity and compaction behavior around the J Sand package. This provides an important link between traditional methods of pressure characterization and numerical modeling. The models also show how the

stress state in the sand and shale change, producing different porosity and permeability behavior than previously thought (Flemings et al., 2001).

Finally, a detailed understanding of the depositional history, regional geology and fluid flow are key to successful pressure prediction. In areas of rapid sedimentation, shallow overpressure precludes traditional pressure prediction techniques when a model is constrained in the shallow subsurface. Additionally, estimation of sand pressure is not accurate if only sand geometry and bounding shale pressure are used to constrain sand overpressure. Overpressure prediction from geometry provides an upper bound for sand overpressure in the salt-seated Bullwinkle basin, but a simple flow model that includes the dynamic effect of the flow field is more effective in matching sand pressure (Figure 2.19).

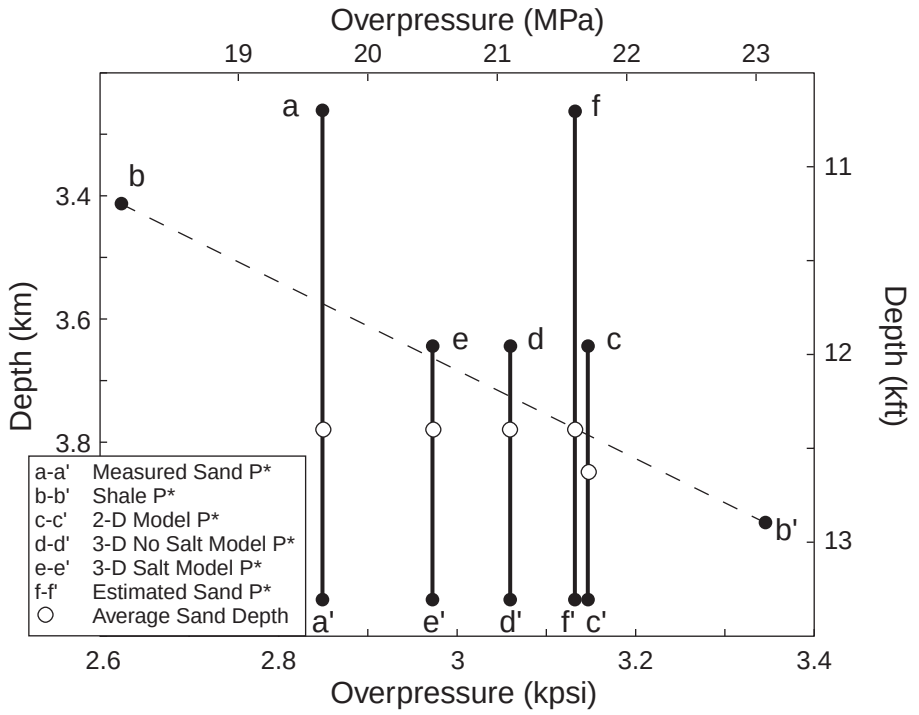

Figure 2.19: Comparison of actual sand overpressure (a-a') to modeled results (Figure 2.17) and the sand overpressure estimated from geometry (Figure 2.18). The models approximate the geometry of the J Sand package by having an equivalent average depth. The shallow, discontinuous portions the J Sand (Figure 2.4) are not included in the models. The 3-D Salt Model (e-e') gives a better prediction of sand overpressure than one that only considers the sand geometry and surrounding shale overpressure (f-f').

Table 2.1: Nomenclature

Variable	Description	Unit
β	Shale compressibility	$M^{-1}LT^2$
f	Acoustic formation factor	
g	Acceleration of gravity	LT^{-2}
ϕ	Porosity	
ϕ_0	Reference porosity	
k	Permeability	L^2
k_x	Horizontal permeability	L^2
k_z	Vertical permeability	L^2
λ^*	Normalized pore pressure ratio	
μ	Viscosity	$ML^{-1}T^{-1}$
P	Pressure	$ML^{-1}T^{-2}$
P_w	Water phase pressure	$ML^{-1}T^{-2}$
P_o	Oil phase pressure	$ML^{-1}T^{-2}$
P_g	Gas phase pressure	$ML^{-1}T^{-2}$
P*	Water phase overpressure	$ML^{-1}T^{-2}$
r	Radius	L
ρ_w	Brine density	ML^{-3}
ρ_o	Oil density	ML^{-3}
ρ_g	Gas density	ML^{-3}
σ_v	Vertical effective stress	$ML^{-1}T^{-2}$
S_v	Vertical stress, overburden	$ML^{-1}T^{-2}$
Δt	Sonic travel-time	TL^{-1}
Δt_{ma}	Shale matrix sonic travel-time	TL^{-1}
z	Depth	L

Table 2.2: Time-Stratigraphic Correlation (Styzen, 1998)

Surface	Name	Marker	Type	Age (Ma)
1	PM 4	*Globorotalia menardii* coiling change	Foraminifera	5.15
2	PM 1R	*Globigerina nepenthes*	Foraminifera	4.2
3	NPM 0	*Reticulofenestra pseudoumbilica*	Nannofossil	3.64
4	NP 3.3	*Sphenolithus neoabies*	Nannofossil	3.47
5	NP 3	*Discoaster tamalis*	Nannofossil	2.78
6	NP 2.9	*Discoaster surculus*	Nannofossil	2.55
7	NP 1.78	*Discoaster brouweri*	Nannofossil	1.95
8	NP 1.68	*Helicosphaera sellii*	Nannofossil	1.41
9	NP 1.55	*Pseudoemiliania 3*	Nannofossil	1.02

Table 2.3: RFT Measurements

Sand	Well	RFT Press. (MPa)	RFT Depth (m TVDSS)	Phase
F	109-1	44.0	2824	Gas
G	109-1	46.8	2999	Water
G2	109-1	52.2	3109	Water
I3A	109-1	56.6	3422	Water
I10	109-1	58.7	3594	Oil
J2	109-1	58.5	3656	Oil
J2	109-1	58.6	3668	Oil
J2	109-1	58.7	3675	Oil
J2	109-1	58.6	3673	Oil
J4	109-1	58.7	3717	Water
J4	109-1	58.8	3725	Water
J2	109-1ST	57.2	3463	Oil
J3	109-1ST	56.7	3491	Gas
I15	64-1-BP	62.3	3505	Gas
J	64-1-BP	68.9	3768	Gas

Table 2.4: Sand Characteristics

Sand	Top (m)	Bottom (m)	OWC (m)	GOC (m)	GWC (m)
F	2758	2926	-	-	2883
G	-	-	-	-	-
G2	2871	3493	-	-	-
I3A	3277	3770	3391	3351	-
I10	3353	3901	3658	-	-
J2	3307	3962	3784	-	-
J3	3353	3962	3612	3503	-
J4	3292	3901	3613	-	-
I15	3429	3783	-	-	-
J Boxer	3560	4267	-	-	3930

Table 2.5: Sand Water Phase Pressure and Overpressure

Sand	RFT Depth (m TVDSS)	Water Phase Pressure (MPa)	Water Phase Overpressure (MPa)	Lithostat (MPa)
F	2824	43.54	13.83	53.99
G	2999	46.82	15.27	57.74
G2	3109	52.20	19.50	60.09
I3A	3422	56.56	20.56	66.96
I10	3594	58.54	20.73	70.79
J2	3656	58.07	19.61	72.20
J2	3668	58.26	19.68	72.44
J2	3675	58.31	19.65	72.60
J2	3673	58.24	19.60	72.55
J4	3717	58.74	19.65	73.49
J4	3725	58.81	19.64	73.66
J2	3463	56.15	19.72	67.86
J3	3491	56.24	19.52	68.49
I15	3505	-	-	70.95
J	3768	68.36	28.73	75.70

Table 2.6: Shale Porosity-Effective Stress Above RFT Measurements

Sand	Effective Stress (MPa)	Shale Porosity
F	10.45	0.240
G	10.92	0.250
G2	7.89	0.270
I3A	10.40	0.247
I10	12.25	0.230
J2	14.13	0.220
J4	14.75	0.215
J2	11.71	0.235
J3	12.25	0.225
J	8.08	0.280

Table 2.7: Average Sand Depth and Overpressure

Sand	Average Depth (m TVDSS)	Estimated Overpressure (MPa)	Percentage of Total Area
J1	3765	21.49	0.15
J2	3785	21.63	0.31
J3 / J4	3815	21.94	0.23
J0	3765	21.47	0.31
Average	3783	21.63	

Chapter 3: Overpressure and Trap Integrity on the Slope of the GOM

3.1. Introduction

A major exploration challenge is to successfully predict the presence of an effective seal. Due to their low permeabilities, high capillary entry pressures and lateral continuity, shales generally form excellent traps. However, even in a shale-rich environment, trap integrity may be compromised by excess fluid pressure. As pressure converges on the least principle stress, processes such as shear failure or hydrofracture may generate fracture permeability (Finkbeiner et al, 2000; Ingram & Urai, 1997). This enhanced permeability facilitates the expulsion of hydrocarbons from a reservoir. We describe with a flow model how pressures at the crests of structures are elevated due to flow focusing. We then document an example in the deepwater GOM where column height may be limited by the stress field. We close with a discussion of how trap integrity can be estimated ahead of the drillbit.

3.2. Flow Focusing

When a dipping, hydrologically continuous sand lies between much lower permeability, overpressured shales, flow focusing occurs (Figure 3.1) (Dugan & Flemings, 2000; Yardley & Swarbick, 2000). In this environment, the vertical pressure gradient in the sand is

approximately hydrostatic, whilst the pressure gradient in the shale is typically near the lithostatic gradient (Figure 3.1). Because of the difference in gradients, pressure at the top of the structure is elevated with respect to the surrounding shale, and pressure low on the structure is depressed. Along a vertical profile penetrating the very center of the sand, pressure remains unchanged (Figure 3.1b). The pressure difference between the sand and shale low and high on the structure drives flow focusing.

The white stream lines in Figure 3.1 depict flow focusing. Flow is driven from regions of high to low pressure. In the undisturbed state (along the edges of the Figure 3.1), flow is nearly vertical in the shales. However, near the sand, stream lines converge into the bottom of reservoir and diverge from the top, recording capture of the flow at the base, focusing of flow along the sand, and expulsion of flow at the crest. This flow modifies the pressure state near the sand. Average sand pressure equilibrates to the average bounding shale pressure, while shale pressure decreases at the bottom of structure and increases at the top.In the subsurface, flow focusing is likely to occur where a ‘binary’ permeability condition exists, e.g. a darcy-range permeability sand surrounded by nano-darcy permeability shales. Because the sand focuses flow, it is crucial that the sand be hydrologically continuous horizontally and vertically. We study flow focusing around a continuous, turbidite sheet sand deposit in the deepwater Gulf of Mexico.

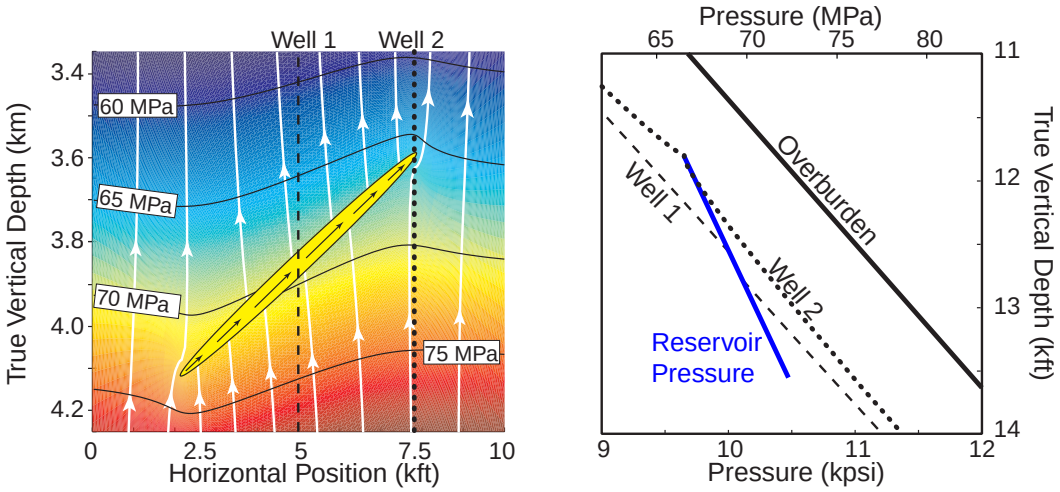

Figure 3.1: Pressure (color and contours) and streamlines (white arrows) around a dipping sand (left). Shale contours dip into the bottom of the sand and are elevated at top of the sand. Along a vertical profile passing through the center of the sand, the pressure gradient is equal to the far field gradient. Fluid enters the bottom of the sand and is focussed along the sand to its crest (black arrows), where it is expelled. The pressure depth plot (right) for the two wells drilled at middle (dashed line) and top of structure (dotted) show very different pressure gradients in the sand and the shale. The vertical pressure gradient in the sand (blue line) is much less than that in the shale. A pressure gradient of 20.8 MPa/km is assumed far from the sand and the pressure at the center of the sand is assumed to equal 69.1 MPa.

3.3. Case study of the J Boxer Sand

We apply this simple 2-D model to a case study of trap integrity on the slope of the GOM, in blocks GC 64 and 65 (the Bullwinkle region) (Figure 3.2). Located in 400 m of water, the Bullwinkle mini-basin is bounded by salt ridges to the west and southeast, with a smaller salt high to the northeast. Along the flanks of the basin, a myriad of normal faults splay off the top of salt. In a west-east cross section, the sands of the Bullwinkle region have a synclinal shape, with nearly 600 m of structural relief (Figure 3.3).

The sediments are clastic deposits of Plio-Pleistocene age and younger. Clay-rich mud-stones are prevalent in the basin, and separate major sands by as much as 150 m. The sed-imentation rate over the past 3.5 Ma has been rapid, averaging around 2 km/my (~2 mm/yr). This high sedimentation history has resulted in little lithification of the sediments and significant generation of overpressure (Holman & Robertson, 1994).

The J Boxer is the principle sand of this case study (Figure 3.3). Based upon 3-D seismic data, the sand has nearly 600 m of structural relief, varying from3550 m depth to over 4100 m (Figure 4). These depths are approximate, as the bottom of the structure lies near the edge of our seismic volume, and the top of the sand may be obscured by the salt body or tuning effects.

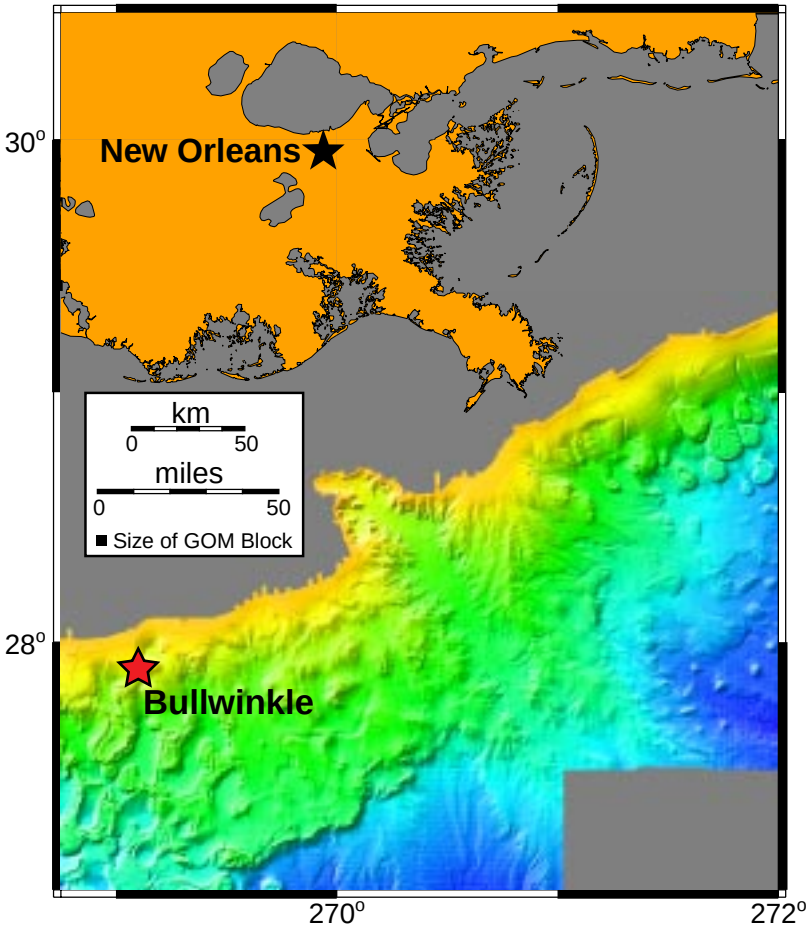

Figure 3.2: Bathymetric map of the slope of the Gulf of Mexico offshore Louisiana. The Bullwinkle Region is located by the red star. The study area is block GC 64 and GC 65 at the top of the slope in approximately 400 m water depth.

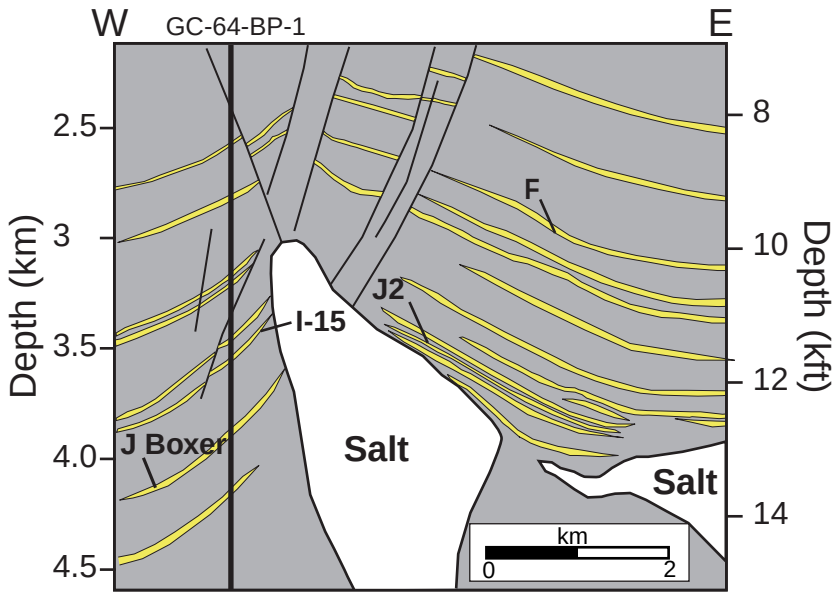

Figure 3.3: Cross section interpreted from depth converted 3-D seismic data. The west-east section runs across the edge of the Bullwinkle basin. The sands (yellow lenses) in the region are synclinal with as much as 600 m of structural relief. The J Boxer sand lies to the west of the Bullwinkle basin.

From an amplitude extraction map of the J Boxer sand, we interpret a 300 m hydrocarbon column trapped by a three-way fault closure at the top of structure (Figures 3.3, 3.4). This interpretation is confirmed by three well penetrations which record the presence of gas either by shows or production (Figure 3.4).

Repeat formation tests (RFTs) taken in the gas leg of the J Boxer sand at the GC 64-1-BP well constrain the pressure in the reservoir (Figure 3.5a). The water phase pressures and the gas pressures are calculated assuming a pressure gradient in the water leg equal to the brine gradient (10.5 MPa/km), and a gradient in the gas column of 2.25 MPa/km (Figures 3.5a). At the top of structure, the gas phase pressure equals 97% of the overburden, and the overburden exceeds the gas phase pressure by only 2.4 MPa (Figure 3.5a, b). This difference between the overburden and pore pressure is referred to as the vertical effective stress.

We predict shale pressures using sonic log velocities. The sonic log of the GC 64-1-BP well, which penetrates the sand just above the midpoint of the structure, is used for the prediction (Hart et al., 1995). This approach relates the consolidation state of the shale, estimated from the velocity, to the shale pressure through a porosity-effective stress model. This model has been applied successfully in the petroleum industry for decades (e.g. Ham, 1966; Eaton 1975), and is well constrained in the Bullwinkle region.

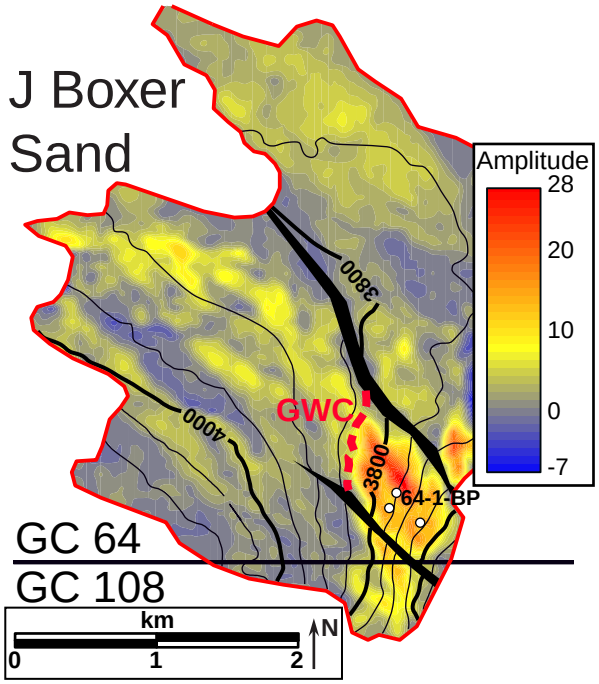

Figure 3.4: Amplitude extraction of the J Boxer sand. Well penetrations are located with white dots. Total structural relief of the sand is ~600 m. The gas-water contact is interpreted to lie at 3840 m depth (red dashed line).

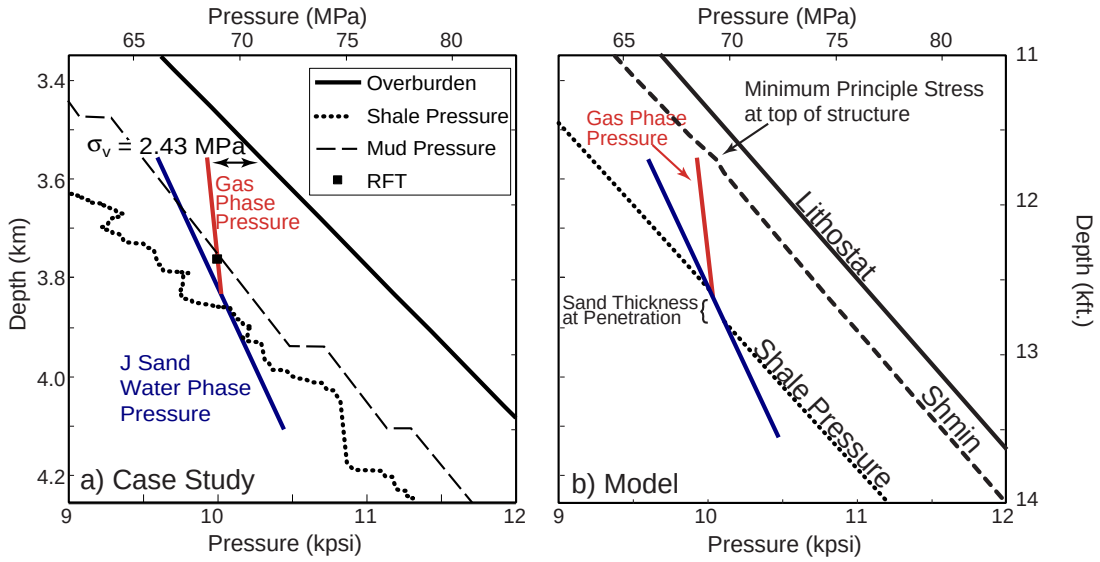

Figure 3.5: a) Pressure-depth plot around the J Boxer sand in GC-64. Predicted shale pressures (dotted line) from well GC 64-1-BP are shown along with the measured pressure and mud pressure. At mid-structure, sand and shale pressures are equal. At top of structure, the vertical effective stress is 2.43 MPa, with gas phase pressure equaling 97% of the overburden. b) Pressure-depth behavior predicted by the analytic model around the J Boxer sand. At top of structure, 0.76 MPa separate the gas phase pressure from the least principle stress, indicating the column is likely stress controlled. Also, as observed at the J Boxer sand, shale pressure equals sand pressure at mid-structure.

At GC 64-1-BP, shale pressures are predicted to parallel the overburden (Figure 3.5a, b). Near the midpoint of the structure, predicted shale pressures match the reservoir water phase pressure. However, at the crest of the structure, shale pressures are predicted to be 4.8 MPa lower than the sand pressure, while at the bottom the inverse is true. These results are consistant with the flow focusing model (Figure 3.1), and suggest flow focusing is controlling the pressure in the sand and bounding shale.

Wireline data and leak off tests (LOTs) constrain stress state at the J Boxer sand. Overburden is calculated by integrating bulk density wireline data (Figure 3.6). Over the depth interval of the sand, the overburden gradient, referenced from the sea-surface, is 19.9 MPa/km. The minimum principle stress is estimated from LOTs. These data all lie near or at the overburden stress, indicating a near isotropic stress state (Figure 3.6). No leak off tests were measured deeper than 2750 m below the mudline. Due to the high degree of scatter and lack of LOTs at the depth of the J, it is difficult to constrain the least principle stress.

When leak off test data are inconsistent, least principle stress is commonly approximated by assuming a constant stress ratio. The stress ratio relates the horizontal effective stress to the vertical effective stress (Pilkington, 1978). In the Bullwinkle region, this only provides a rough estimate of least principle stress, as the relationship to the overburden is likely not constant near a dynamic salt dome. The shale pressure at top of structure and the overburden are used to calculate least principle stress assuming a stress ratio of 0.7.

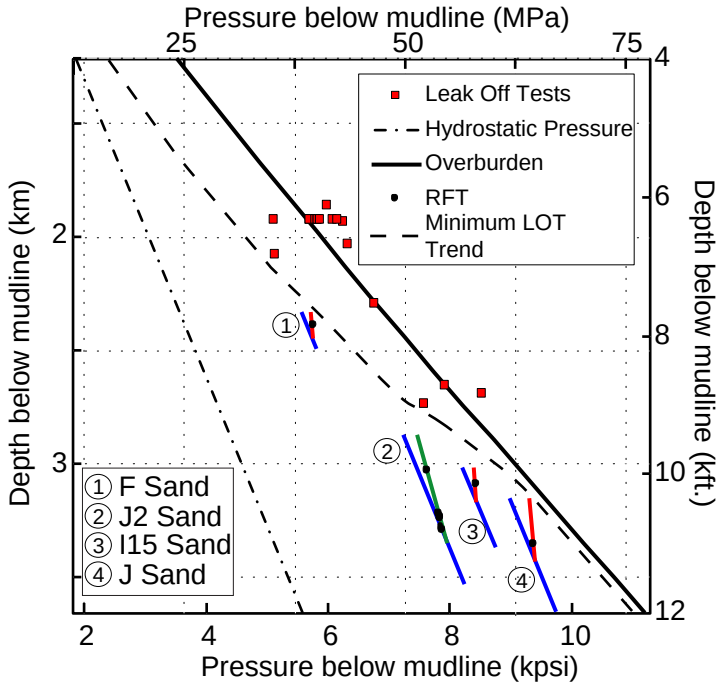

Figure 3.6: Pressure-depth plot illustrating the stress and pressure state of some major sands in the Bullwinkle region. Pressure in the sands are constrained by repeat formation tests (RFTs). Least principle stress is estimated from leak off tests (LOT). The minimum LOT trend represents the lowest estimated value of the least principle stress. Although no LOT measurements exist at the J Boxer sand (4) depth, we interpret a stress by assuming that the gas column is stress limited.

We specify an overburden gradient of 19.9 MPa/km to top of structure and far field shale pressure gradient of 20.8 MPa/km. The model predicts that at the top of the sand, flow focusing has elevated bounding shale pressure (see Figure 3.1). This elevation in pressure leads to a shift in the modeled least principle stress at top of structure. With this shift, gas phase pressure at the top of the reservoir is estimated to be about 0.7 MPa less than the modeled least principle stress (Figure 3.5b).

3.4. Discussion

Although the mudrocks in the Bullwinkle region form effective seals, as the substantial discovery made at Bullwinkle indicates, some evidence for hydrocarbon loss exists. This includes fluid expulsion features on the sea-floor and zones of seismic washout overlying some of the reservoir sands (Figure 3.7). Two mechanisms for fluid expulsion that we consider are dilatant hydrofracture and shear failure along pre-existing faults (Finkbeiner et al., 2000). Both mechanisms are triggered as the hydrocarbon phase pressure converges on the least principle stress. As hydrocarbons charge the sand, fluid pressures at top of structure are gradually raised due to the incoming flux of gas and the lower fluid pressure gradient of the gas (Schowalter, 1976). The height of the hydrocarbon column will be controlled by flow along the fracture; at high enough pressures, the fracture may slip or dilate, allowing hydrocarbons to escape (Figure 3.8). This reduces the pressure at top of structure and reseals the trap.

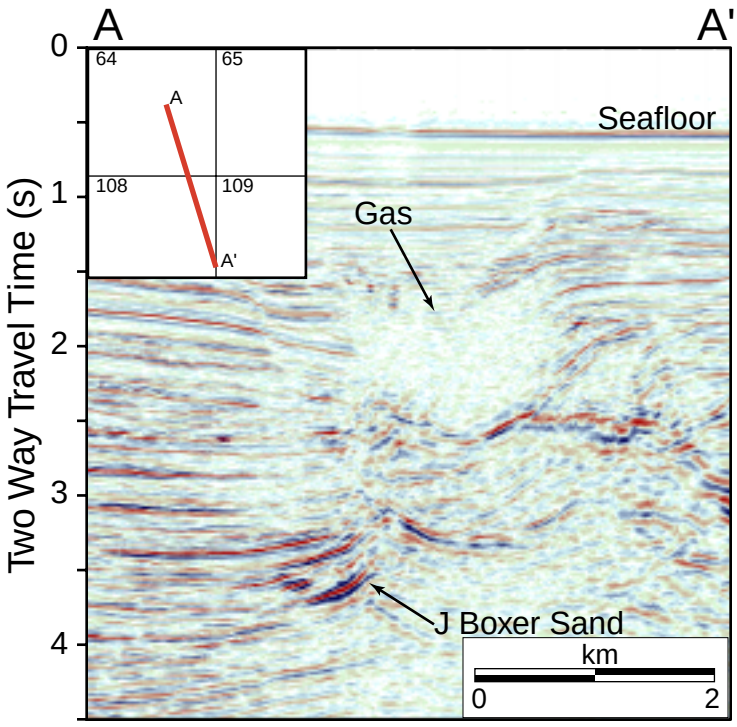

Figure 3.7: Example of seismic washout that is interpreted to be indicative of gas along a N-S seismic profile. The gas decreases the impedance contrast between the sediments resulting in a light area with no reflectors on seismic data. We interpret that the gas has leaked from the underlying J Boxer sand.

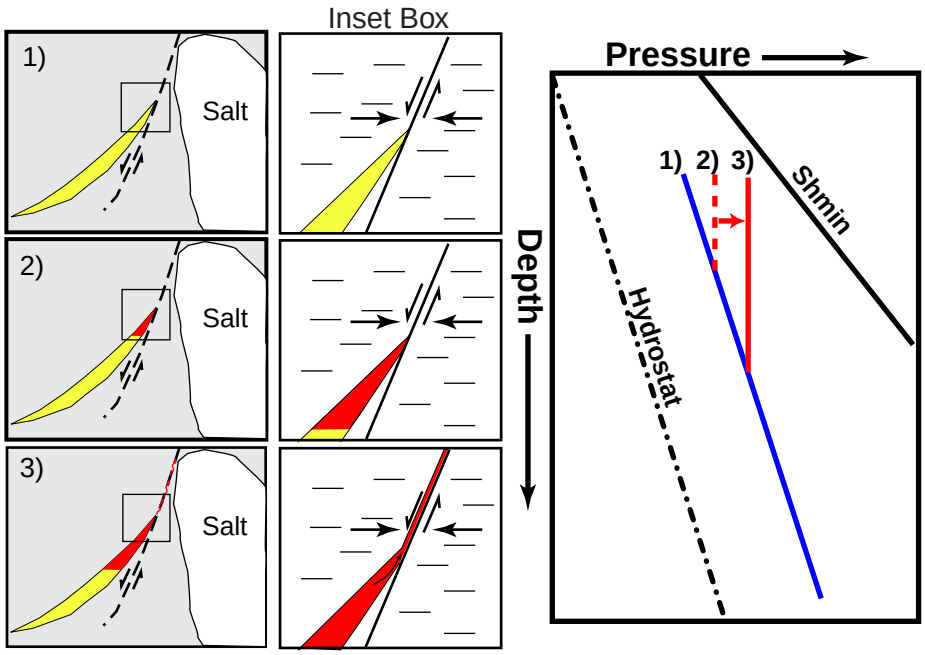

Figure 3.8: Cartoon charge history of the J Boxer sand. As gas charges the sand, pressure at the top of the structure is increased because of the lower pressure gradient of the gas (2,3). At some critical pore pressure the fault or fracture will dilate and allow gas to escape (3).

At the J Boxer sand one hypothesis is that the column height is being stress controlled in this fashion. Although the pressure at top of the gas column does not reach the least principle stress, the small effective stress at top of structure and the fact the trap is not filled to spill can be interpreted to mean that the column is stress-controlled. The large structural relief of the sand and the flow focusing effect drive the sand pressure towards trap failure as high pressures from deep are transferred upstructure. Any additional hydrocarbon input into the sand results in fluid expulsion, with gas phase pressure initiating hydraulic fracture or shear failure.

An alternative hypothesis is that the J Boxer sand is not leaking, and is a portion of a more complicated structure, such as a protected trap (Mann & Mackenzie, 1990). For example, consider a protected trap where one limb of a charged sand is structurally higher than another (Figure 3.9). Although the limbs are hydraulically connected, very different column heights may exist in the two structures. In the larger, more promising limb, water phase pressures are ~0.7 MPa less than the least principal stress. A 45 m gas column can be held by this structure; additional hydrocarbon input breaches trap integrity and hydrocarbons escape. However, because the smaller limb is structurally lower, the water phase pressure at the top of this structure is much less than the fracture pressure (Figure 3.9). This secondary structure is able to fill to its spill point, and hold a gas column of 225 m.

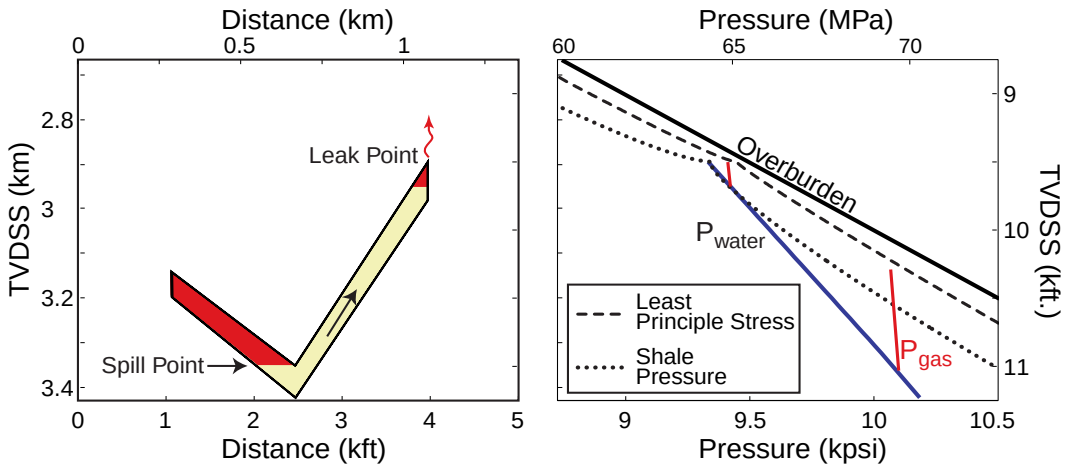

Figure 3.9: A schematic cross section of a protected trap and its pressure-depth plot. Although the limbs are hydraulically connected, the larger limb is unable to hold a significant hydrocarbon column as higher pressures are transferred from the base to the top of the structure. Because of this, the water phase pressure (P_{water}) at top of structure is only 0.7 MPa from the fracture pressure. Any additional hydrocarbon input will result in shear failure or hydraulic fracturing, and the expulsion of hydrocarbons. The deeper, smaller limb is able to fill to the spill point. The water phase pressure at the top of the smaller structure is 2.75 MPa lower than the fracture pressure because of the low pressure gradient within the sand.

It is straightforward to apply the flow focusing concept to assess maximum column height and trap integrity. In the exploration of frontier basins, the use of seismic and analog data can provide all the information necessary to perform the analysis. Structural relief can be estimated from seismic data. Shale pressure can be estimated from the seismic interval velocities, and as our case study suggests, sand pressure can be estimated using the shale pressure at mid-structure. The overburden stress can be estimated from either analog data or velocity. Least principle stress estimates can be made using a constant stress ratio.

If seismic coverage is minimal, but nearby well control is available, either *in situ* data or wireline measurements can be used to estimate sand pressure and the overburden. Repeat formation tests or calculated shale pressures from the sonic log can be used to estimate sand pressure. The density log can be integrated to find the overburden. Fracture pressure can be estimated from leak off test data or by assuming a stress ratio. Finally, if a leak point can be found in an extensive sand body, it is only necessary to constrain the overburden, stress ratio and the height of the stress controlled column to estimate column height anywhere in the sand. Fracture pressure and sand pressure can be backed out from these data. Once the fracture and sand pressure are known, trap integrity can be predicted for secondary structures.

3.5. Conclusions

A simple analytical flow model combined with a case study offshore GOM illustrates the importance of flow focusing when assessing hydrocarbon column heights and trap integrity. In a clay-rich, highly geopressured environment, subtle changes in the reservoir orientation can lead to significant variation in the sand pressure, and thus the column height trapped within a reservoir sand. By channeling fluids from the shales low on structure to high, flow focusing elevates pressures on top of structure, often bringing pressure perilously close to the least minimum stress. However, by understanding the structure of the sand body and how to best estimate sand pressure from shale pressure predictions, one can account for this effect in their risk assessment. As the petroleum industry moves to deeper and more technically challenging targets, flow focusing may prove a critical tool in risk analysis.

Appendix A: Geometrical Sand Pressure Prediction Method

A.1. Introduction

Steady-state fluid flow modeling (Stump & Flemings, 2000; Lupa et al., 2002; Chapter 2) suggest that sand overpressure is closely related to its geometry and the surrounding shale pressure, and can subsequently be predicted from them. We use 3-D seismic data to estimate sand geometry and estimate sand overpressure. We then compare this estimate to measured sand pressure data from RFTs (Repeat Formation Tests).

We consider the hydraulically connected J Sand package in the Bullwinkle basin (J0-J4) and the J Boxer for this exercise (Holman & Robertson, 1994; Kikani & Smith, 1996). The Bullwinkle sands were mapped using Geco-Prakla's 1995 3-D survey by Alastair Swanston (Swanston, 2001), and the J Boxer by myself using the Bull35 3-D survey. In the survey, Swanston (2001) was not able to pick separate reflectors for the J3 / J4 sands and the I10 / J0 sands. We simplify this by assuming that the J3 and J4 are of equivalent size, and the reflector represents their average depth and assume the I10/J0 reflector is one hydraulically connected sand.

A.2. Average Sand Depth

The average depth of each sand is calculated using the Landmark utilities Zmap and TDQ. The sands are first depth converted using check shot data in TDQ, and corrected using well penetrations with Zmap. Average sand depth is found by gridding the data and taking the average of the nodes (Table A.1) (Figure A.1). The J Sand package in the Bullwinkle basin has an average depth of 3785 m TVDSS and the J Boxer, 3900 m TVDSS.

A.3. Sand Overpressure Prediction

Pressure in the sand is estimated from the surrounding shale pressure. It is desirable for this step to have seismic overpressure cube around the sand. This allows the average overpressure to be found in much the same way as the average sand depth was found, by extracting an overpressure horizon and averaging it. However, a seismic overpressure cube is unavailable in our basin. Instead we use the overpressures predicted from well data.

For the J Boxer, we have a shale pressure estimate at only 1 well, the GC-64-1-BP. Predicted shale pressure equals water phase sand pressure near the midpoint of the sand. If the geometry of the sand is used to estimate pressure within the sand, we find a similar result (Figure 2). We estimate a sand overpressure of ~29 MPa compared to the measured overpressure of 28.7 MPa.

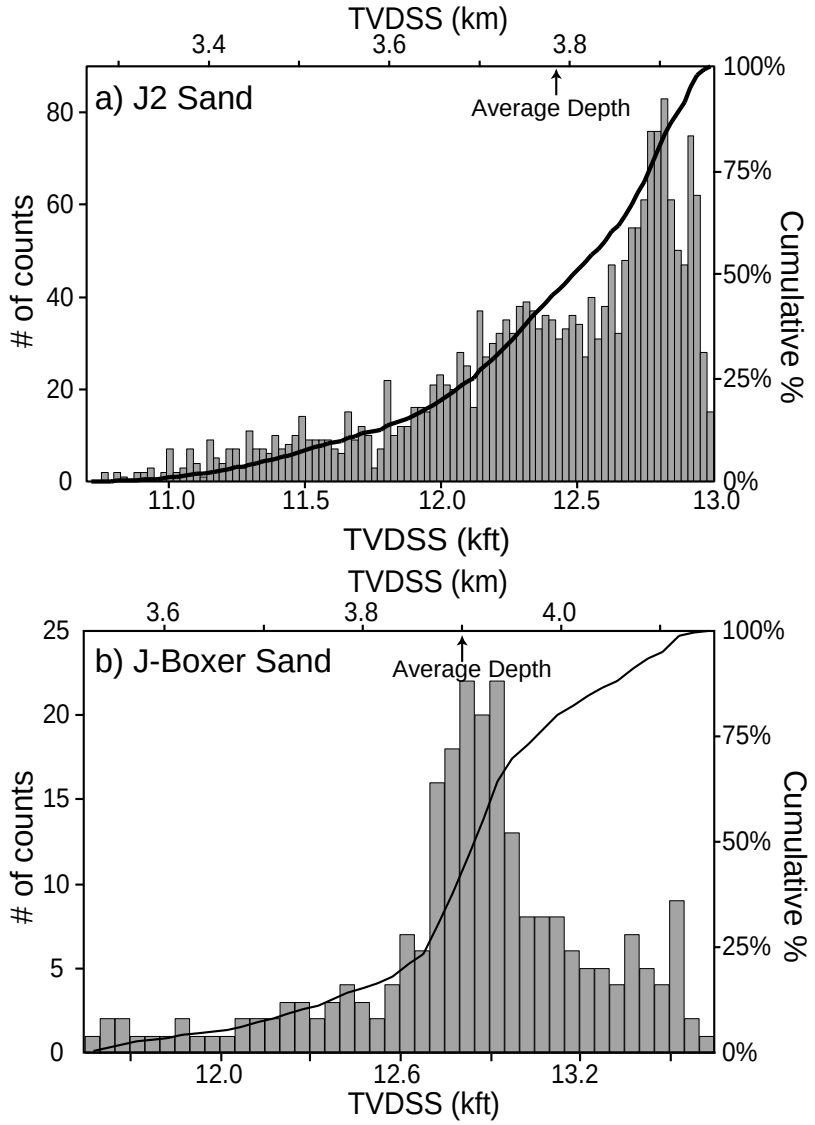

Figure A.1: Examples of areal depth distribution for the a) J2 Sand and b) J Boxer Sand. The sand horizon were gridded into equal area sections in map view to find average depth. The J2 sand has an average depth of 3.8 km TVDSS, and the J Boxer of 3.9 km TVDSS (Table A.1).

For the J Sands in the Bullwinkle basin, we found an overpressure datum from a group of wells. From this datum, we extrapolated the overpressure at the average depth of the sand using the far-field overpressure gradient,

$$SandP^* = P^*_{datum} + \left(\frac{P^*}{z}\right)_{farfield} \bar{z}_{sand}. \quad \text{(A.1)}$$

This approximates the original shale pressure condition below flow focussing occurs. One assumption of this method is that all the surrounding shale has been able to flow into the sand and that its pressure is recharged from the far-field throughout the basin history.

The overpressure datum is set at 2750 m TVDSS. Overpressure at this depth varies from a maximum of 12.5 MPa to a minimum of 11.2 MPa, with an average of 11.7 MPa. The overpressure gradient suggested by the well data is 9.62 MPa/km (90% of overburden gradient). We estimate a shale overpressure between 21.47 MPa to 21.6 +/- 0.7 MPa at the average depths of the J Sands (Table A.1). Weighting the sands by their size and averaging, we estimate a J Sand overpressure of 21.63 MPa. Measured water phase sand overpressure is 19.65 MPa (Figure 3). In terms of mudweight, using this method of estimating pressure, we would overestimate sand pressure near the top of structure at 3350 m by 0.5 ppg. There are two obvious possibilities for this mismatch; the sands are mapped incorrectly or the pressure prediction is wrong. However, we are confident that the mapping is correct and in our pressure prediction.

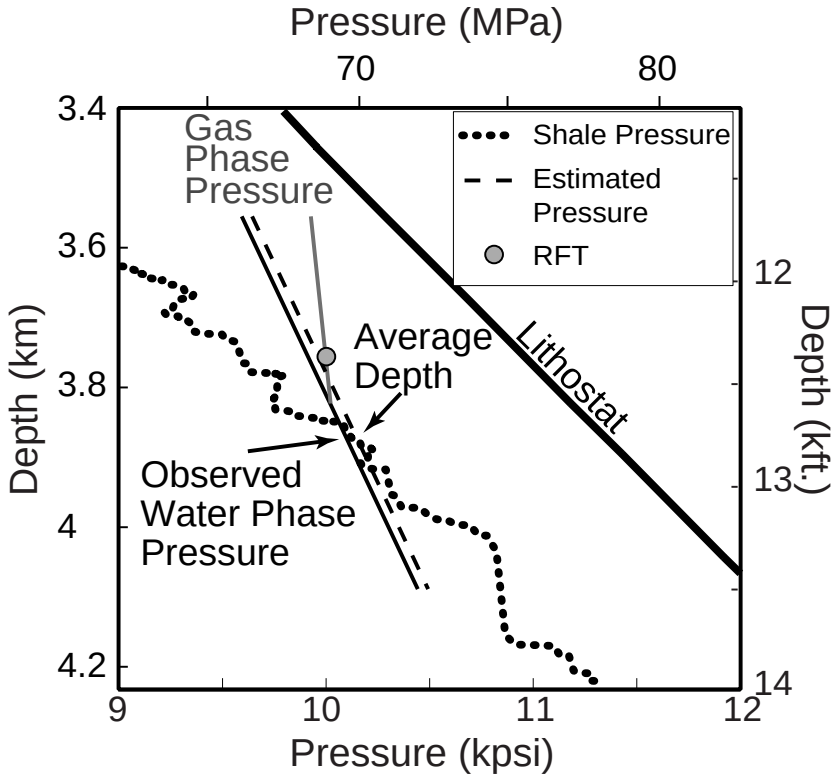

Figure A.2: Estimated water phase pressure for the J Boxer sand compared to that calculated from an RFT measurement. We assume that sand pressure is equal to shale pressure at the sand's average depth. Shale pressure is predicted from the GC-64-1-BP well using the Shallow Overpressure approach (see Chapter 2).

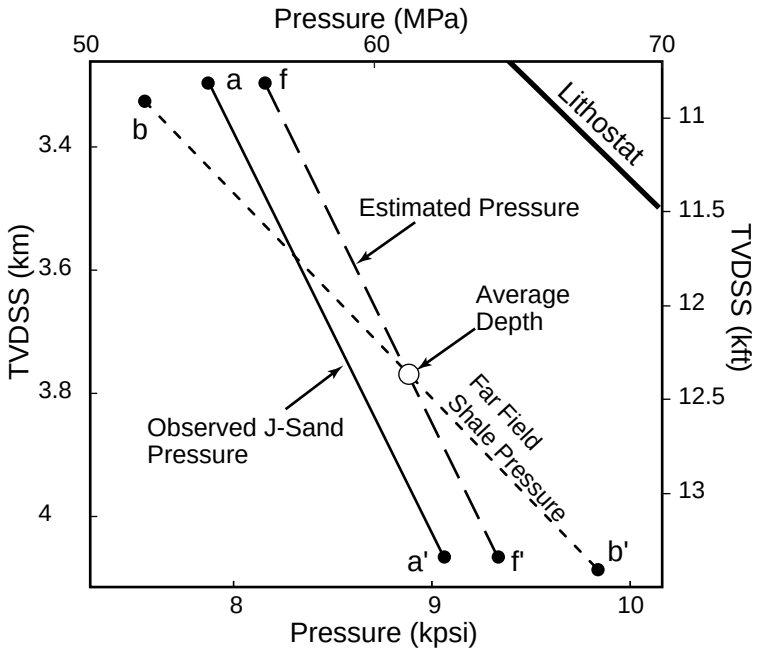

Figure A.3: Comparison of measured water phase pressure in the J Sand package and the pressure estimate from geometry. The assumption that sand and shale pressure are equal at the average depth does not work for the J Sands.

An alternative possibility is that the mismatch is due to the hydrogeologic behavior of the basin. We are able to effectively predict pressure from geometry in the J Boxer, but not the J Sands. The J Boxer lies in a relatively simple geologic setting compared to the J Sands, which are underlain by salt. The shale may not be recording the pressure effect of salt. Instead the shale may still be draining where we constrain shale pressure. Unfortunately we do not model the time dependant behavior of the basin, so we can no make firm conclusions. Further work would include modeling the basin with a time dependant model and including bed parallel anisotropy to constrain the behavior of the shale above the sand.

A.4. Conclusions

Sand pressure predicted from sand geometry is much higher than that observed for the J Sands in the Bullwinkle basin. The method used may be too simple, as it doesn't consider much of the geological complexity of the basin or the dynamic flow behavior around the sand. In more complex geologic settings, pressure prediction by this simple method may not be effective.

Table A.1: Average Sand Depth and Overpressure

Sand	Average Depth (m TVDSS)	Estimated Overpressure (MPa)	Percentage of Total Area
J1	3765	21.49	0.15
J2	3785	21.63	0.31
J3 / J4	3815	21.94	0.23
J0	3765	21.47	0.31
J Sand Average	3785	21.63	-
J Boxer	3900	28.97	1

Appendix B: Derivation of the Cylindrical LaPlace Equation and Finite Difference Approximation

B.1. Derivation of the Cylindrical LaPlace Equation

To represent the Bullwinkle basin, we construct a steady state fluid flow model using the radial diffusion equation. To derive the radial diffusion equation, we build upon first principles assuming a constant fluid density, isotropic and heterogeneous permeability and dr, dz are constant in time (Figure B.1). Water is the only phase present in the system. From Darcy's Law, we can solve for the volumetric water flux in the radial and vertical direction.

$$Q_r = -\frac{k}{\mu} 2\pi r dz \frac{\partial P^*}{\partial r}, \tag{B.1}$$

and

$$Q_z = -\frac{k}{\mu} 2\pi r dr \frac{\partial P^*}{\partial z}. \tag{B.2}$$

Conservations of mass dictates that the time rate of change of mass in a certain volume is the difference between the flux entering the volume and the flux leaving the volume, or

$$TROCM = FluxIn_{r,z} - FluxOut_{r,z}. \tag{B.3}$$

In Eq. (B.3),

$$TROCM = \frac{\partial \rho 2\pi r dr dz \phi}{\partial t}, \tag{B.4}$$

$$FluxIn_{r,z} = Q_r \rho + Q_z \rho, \tag{B.5}$$

and

$$FluxOut_{r,z} = Q_r\rho + Q_z\rho + \frac{\partial(Q_r\rho)}{\partial r}dr + \frac{\partial(Q_z\rho)}{\partial z}dz \quad . \tag{B.6}$$

If Q_r and Q_z are substituted from Eqs. (B.1) and (B.2) into the definitions of *TROCM*, $FluxIn_{r,z}$, and $FluxOut_{r,z}$, then equation (B.3) equals

$$\frac{\partial\rho 2\pi r dr dz\phi}{\partial t} = -\left[\frac{\partial\left(\left(-\frac{k}{\mu}2\pi r dz\frac{\partial P^*}{\partial r}\right)\rho\phi\right)}{\partial r}dr + \frac{\partial\left(\left(-\frac{k}{\mu}2\pi r dr\frac{\partial P^*}{\partial z}\right)\rho\phi\right)}{\partial z}dz\right]. \tag{B.7}$$

Simplifying this in two steps, and assuming porosity is approximately constant, we find

$$r\phi\frac{\partial\rho}{\partial t} = K\frac{\partial}{\partial r}\left(r\frac{\partial P^*}{\partial r}\right) + K\frac{\partial}{\partial z}\left(r\frac{\partial P^*}{\partial z}\right), \tag{B.8}$$

and then,

$$\phi\frac{\partial\rho}{\partial t} = 0 = \frac{1}{r}\left(K\frac{\partial r}{\partial r}\frac{\partial P^*}{\partial r} + Kr\frac{\partial^2 P^*}{\partial r^2} + K\frac{\partial r}{\partial z}\frac{\partial}{\partial z}P^* + Kr\frac{\partial^2 P^*}{\partial z^2}\right), \tag{B.9}$$

where

$$K = \frac{k\rho g}{\mu}, \tag{B.10}$$

and

$$\frac{\partial r}{\partial z} = 0. \tag{B.11}$$

This yields the diffusion equation used for our steady state flow model,

$$0 = K\frac{\partial^2 P^*}{\partial r^2} + K\frac{\partial^2 P^*}{\partial z^2} + \frac{K}{r}\frac{\partial P^*}{\partial r} \quad . \tag{B.12}$$

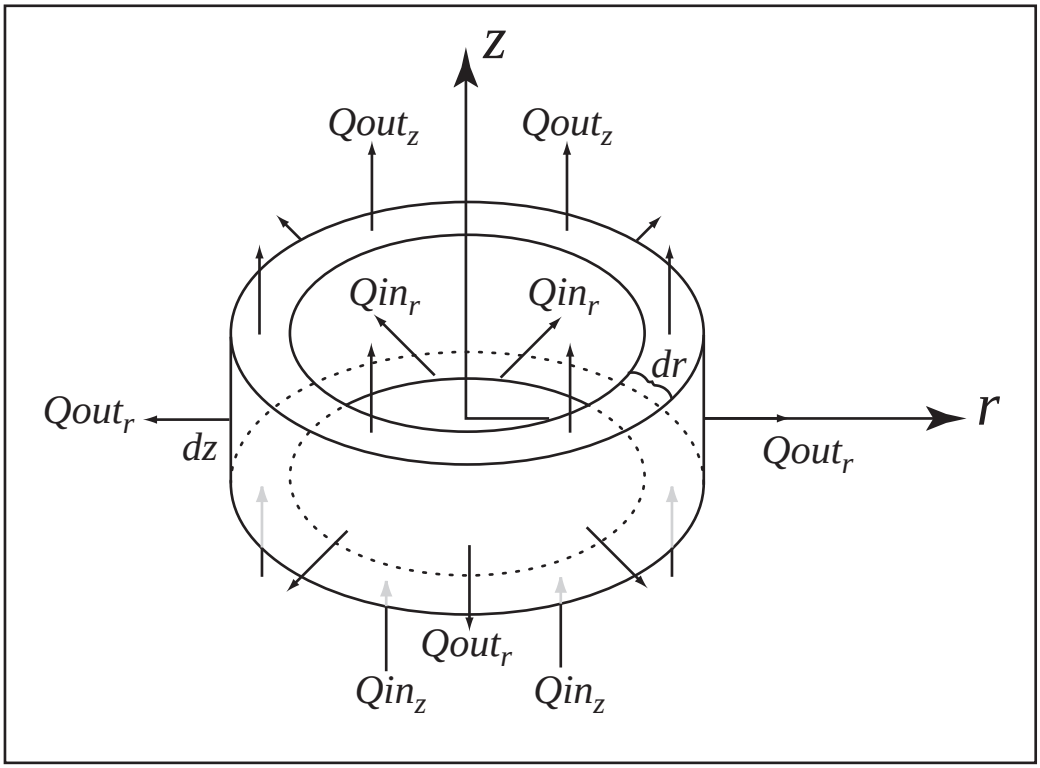

Figure B.1: The geometry and the variables considered in the radial flow solution. The model assumes radial symmetry with flow in both the vertical and radial directions.

B.2. Finite Difference Approximation

To model Eq. (B.12) we use a finite volume approximation (Figure B.2). Once again we only consider the water phase and assume radial symmetry. Since this is a radial solution with flow possible in only the radial and vertical directions, we have three possible areas in our finite volume for flow to pass through. These areas are the back, the front and the equivalent areas of the top and bottom.

$$Ain_r = 2\pi\left(r_{i,j} - \frac{1}{2}\Delta r\right)\Delta z, \tag{B.13}$$

$$Aout_r = 2\pi\left(r_{i,j} + \frac{1}{2}\Delta r\right)\Delta z \tag{B.14}$$

and

$$A_z = 2\pi r_{i,j}\Delta r\Delta z. \tag{B.15}$$

After Ertekin (2001), we use the harmonic averages of the hydraulic conductivity for the adjacent volumes to solve for the conductivity in and out of the volumes.

$$\frac{1}{Kin_r} = \frac{1}{2}\left(\frac{1}{K_{i,j}} + \frac{1}{K_{i-1,j}}\right), \frac{1}{Kout_r} = \frac{1}{2}\left(\frac{1}{K_{i,j}} + \frac{1}{K_{i+1,j}}\right) \tag{B.16}$$

$$\frac{1}{Kin_z} = \frac{1}{2}\left(\frac{1}{K_{i,j}} + \frac{1}{K_{i,j-1}}\right), \frac{1}{Kout_z} = \frac{1}{2}\left(\frac{1}{K_{i,j}} + \frac{1}{K_{i,j+1}}\right). \tag{B.17}$$

To approximate the right side of Eq. (B.12) we use the law of Conservation of Mass for each term. For the radial darcy flow term, $K\frac{\partial^2 P^*}{\partial r^2}$:, we set

$$FluxIn - FluxOut = Kin_r Ain_r \left(\frac{P^*_{i-1,j} - P^*_{i,j}}{\Delta r^2} \right) - Kout_r Aout_r \left(\frac{P^*_{i,j} - P^*_{i+1,j}}{\Delta r^2} \right)$$

. (B.18)

For the approximation of the vertical darcy flow term, $K \frac{\partial^2 P^*}{\partial z^2}$:, we set

$$FluxIn - FluxOut = Kin_z A_z \left(\frac{P^*_{i,j-1} - P^*_{i,j}}{\Delta z^2} \right) - Kout_z A_z \left(\frac{P^*_{i,j} - P^*_{i,j+1}}{\Delta r^2} \right). \quad (B.19)$$

Finally, to approximate the velocity decrease due to radial spreading, $\frac{K}{r} \frac{\partial P^*}{\partial r}$:, we set

$$FluxIn - FluxOut = \frac{Kin_r Ain_r}{r_{i,j} - \frac{1}{2}\Delta r} \left(\frac{P_{i-1,j} - P_{i,j}}{\Delta r} \right) - \frac{Kout_r Aout_r}{r_{i,j} + \frac{1}{2}\Delta r} \left(\frac{P_{i,j} - P_{i+1,j}}{\Delta r} \right). \quad (B.20)$$

Combining the Eqs. (II.6), (II.7) and (11.8) and rearranging we find

$$\begin{aligned} 0 = & -(P_{i,j}) \left(\frac{Kin_r Ain_r + Kout_r Aout_r}{\Delta r^2} + \frac{Kin_z A_z + Kout_z Aiz_z}{\Delta z^2} \right. \\ & \left. + \frac{Kin_r Ain_r}{r_{i,j}\Delta r - \frac{1}{2}\Delta r^2} + \frac{Kin_r Ain_r}{r_{i,j}\Delta r + \frac{1}{2}\Delta r^2} \right) + (P_{i-1,j}) \left(\frac{Kin_r Ain_r}{\Delta r^2} + \frac{Kin_r Ain_r}{r_{i,j}\Delta r - \frac{1}{2}\Delta r^2} \right) \\ & + (P_{i+1,j}) \left(\frac{Kout_r Aout_r}{\Delta r^2} + \frac{Kout_r Aout_r}{r_{i,j}\Delta r + \frac{1}{2}\Delta r^2} \right) + (P_{i,j-1}) \left(\frac{Kin_z A_z}{\Delta z^2} \right) \\ & .. \\ & + (P_{i,j+1}) \left(\frac{Kout_z A_z}{\Delta z^2} \right) \end{aligned} \quad (B.21)$$

This is the equation used in the radial flow model.

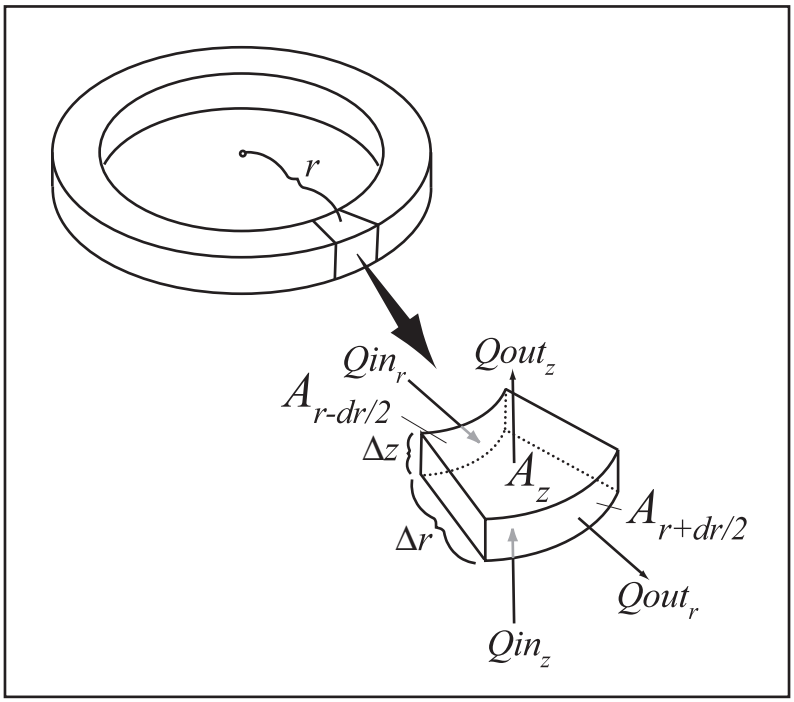

Figure B.2: Assumptions and geometry for the finite difference scheme.

Table B.1: Appendix Nomenclature

Variable	Description	Unit
ϕ	Porosity	
Ain_r	Cross sectional area in r direction into finite volume	L^2
$Aout_r$	Cross sectional area in r direction out of finite volume	L^2
A_z	Cross sectional area in z direction in and out of finite volume	L^2
Δr	Finite step in r direction	L
Δz	Finite step in z direction	L
dr	Incremental lengths in r direction	L
dz	Incremental length in z direction	L
k	Permeability	L^2
K	Hydraulic conductivity	LT^{-1}
Kin_r,$Kout_r$	Hydraulic conductivities going into and out of finite volume in r direction	LT^{-1}
Kin_z,$Kout_z$	Hydraulic conductivities going into and out of finite volume in z direction	LT^{-1}
$K_{i,j}$	Hydraulic conductivity at node i, j	LT^{-1}
μ	Fluid viscosity	$ML^{-1}T^{-1}$
g	Acceleration of gravity	LT^{-2}
P	Pressure	$ML^{-1}T^{-2}$
Pc	Pressure at midpoint between two nodes	$ML^{-1}T^{-2}$
P*	Overpressure	$ML^{-1}T^{-2}$
$P^*_{i,j}$	Overpressure at node i, j, where i is	$ML^{-1}T^{-2}$
$Q_{r,z}$	Volumetric water flux in r and z directions	L^3T^{-1}
ρ	Fluid density	ML^{-3}
$r_{i,j}$	Radius to node i, j	L
TROCM	Time rate of change of mass	MT^{-1}

Table B.1: Appendix Nomenclature

Variable	Description	Unit
u	Radial fluid velocity	LT^{-1}
w	Vertical fluid velocity	LT^{-1}
ψ_s	Stokes stream function	
z	Depth	L

Appendix C: Derivation of Radial Stream Function

C.1. Stokes Stream Function

To explore the flow regime of the Bullwinkle basin, we calculated streamtubes in 3-D. We followed Phillips' (1991) derivation of the Stokes stream function to solve for the stream-tubes. In cylindrical coordinates, the incompressibility condition is,

$$\nabla \cdot u = \frac{1}{r}\frac{\partial}{\partial r}(ru) + \frac{1}{r}\frac{\partial v}{\partial \theta} + \frac{\partial w}{\partial z}. \tag{C.1}$$

If flow is axially symmetric, the basic assumption of our 3-D flow model, there is no flow in the θ direction, e.g. $\frac{\partial}{\partial \theta} = 0$, and

$$0 = \frac{1}{r}\frac{\partial}{\partial r}(ru) + \frac{\partial w}{\partial z}. \tag{C.2}$$

This is satisfied by the function ψ_s, the Stokes stream function, such that

$$u = \frac{1}{r}\frac{\partial \psi_s}{\partial z}, \quad w = -\frac{1}{r}\frac{\partial \psi_s}{\partial r}. \tag{C.3}$$

This velocity in the radial and vertical direction is related to the gradient of the stream function in the perpendicular direction, decreasing with increasing radius. From Darcy's law, we also know the velocity is proportional to the overpressure gradient.

$$w = -\frac{k}{\mu}\frac{\partial P^*}{\partial z}. \tag{C.4}$$

If we substitute Eq. (C.4) into Eq. (C.3),

$$-\frac{k}{\mu}\frac{\partial P^*}{\partial z} = -\frac{1}{r}\frac{\partial \psi}{\partial r} \tag{C.5}$$

overpressure is related to the stream function. More importantly, the solution for the overpressure field (Appendix B) can be used to solve for the stream function, where

$$r\frac{w}{\mu}\frac{\partial}{\partial z}P^{*}\partial z = \partial\psi \tag{C.6}$$

and,

$$\int r\frac{K}{\mu}\frac{\partial P^{*}}{\partial z}\partial z = \int rw\partial z = \int\partial\psi = \psi\ . \tag{C.7}$$

C.2. Finite Difference Solution

To apply Eq. (C.7) to our flow model, it is necessary to consider that permeability changes halfway between each finite difference point, at the edge of each finite volume. To account for this, we solve for the pressure at the horizontal edges of each finite volume (*Pc**). From Darcy's law and conservation of mass, we know that the flux just before and after the boundary are equal, and as area is constant, w_1=w_2. Thus

$$w_1 = -\frac{k_1}{\mu}\left(\frac{P_1^{*} - Pc^{*}}{dz}\right) = w_2 = -\frac{k_2}{\mu}\left(\frac{P_2^{*} - Pc^{*}}{dz}\right). \tag{C.8}$$

Rearranging and solving for *Pc**, we find

$$Pc^{*} = \frac{(P_1^{*}k_1 + P_2^{*}k_1)}{k_1 + k_2}, \tag{C.9}$$

or in terms of our matrices,

$$Pc^{*}_{i,\,j} = \frac{(P_{i,\,j}^{*}k_{i,\,j} + P_{i+1,\,j}^{*}k_{i+1,\,j})}{k_{i,\,j} + k_{i+1,\,j}}. \tag{C.10}$$

Velocity is then calculated using Eq. (C.4) from each horizontal finite volume boundary to the underlying node,

$$w_{i,j} = k_{i,j}(Pc^*_{i,j} - P_{i,j}^*)\,. \tag{C.11}$$

Equation (C.7) states that the stream function is the simply integral of the velocity in the radial direction, which for our finite difference solution is equivalent to the summation of each row of nodes in the radial direction. The solution can be visualized by simply contouring the stream function.

References

Best, K.D. (2002). Development of an Integrated Model for Compaction/Water Driven Reservoirs and its Application to the J1 and J2 Sands at Bullwinkle, Green Canyon Block 65, Deepwater Gulf of Mexico. Masters Thesis, Penn State University, 264 p.

Bethke, C. M. (1986). Inverse Hydrologic Analysis of the Distribution and Origin of Gulf Coast-Type Geopressured Zones. *Journal of Geophysical Research, 91*(B6), 6535-6545.

Bird, R.B., Sterwart, W.E. & Lightfoot, E.N. (1960). *Transport Phenomena*. John Wiley & Sons, New York. 780 p.

Bowers, G. (2001). Determining an Appropriate Pore-Pressure Estimation Strategy. In *2001 Offshore Technology Conference, Paper 13042*.

Bowers, G. (1994). Pore Pressure Estimation from Velocity Data: Accounting for over-pressure mechanisms besides undercompaction. *Society of Petroleum Engineers, Paper SPE 27488*, 515-529.

Comisky, J.T. (2001). Petrophysical Analysis and Geologic Model for the Bullwinkle J Sands with Implications for Time-Lapse Reservoir Monitoring, Green Canyon Block 65, Offshore Louisiana. Masters Thesis, Penn State University, 134 p.

Darby, D., Haszeldine, R.S., & Couples, G.D. (1998). Central North Sea overpressures: insights into fluid flow from one- and two-dimensional basin modelling. In *Basin Modelling: Practice and Progress, Geological Society, London, Special Publications, 141,* 95-107.

Dugan, B. & Flemings, P. B. (2000). Overpressure and Fluid Flow in the New Jersey Continental Slope: Implications for Slope Failure and Cold Seeps. *Science, 289,* 281-291.

Eaton, B. (1975). The Equation for Geopressure Prediction from Well Logs. *Society of Petroleum Engineers, Paper SPE 5544*.

Ertekin, T., Abou-Kassem, J.H. & King, G.R. (2001). *Basic Applied Reservoir Simulation*. Society of Petroleum Engineers Inc., Richardson, TX.

Finkbeiner, T., Zoback, M., Stump B.B., & Flemings, P.B. (2001). Stress, Pore Pressure, and Dynamically Constrained Hydrocarbon Columns in the South Eugene Island 330 Field, Gulf of Mexico. *American Association of Petroleum Geologists Bulletin, 85*(6), 1007-1031.

Flemings, P. B., Comisky, J.C., Liu, X., & Lupa, J.A. (2001). Stress-Controlled Porosity in Overpressured Sands at Bullwinkle (GC 65), Deepwater Gulf of Mexico. In *2001 Offshore Technology Conference, Paper 13103*.

Flemings, P. B., Stump, B. B., Finkbeiner, T., & Zoback, M. (in press). Overpressure and Flow-Focusing in the Eugene Island 330 field (Offshore Louisiana, U.S.A.): Theory, examples, and implications. *American Journal of Science*.

Gibson, R.E. (1958). The Process of Consolidation in a Clay Layer Increasing in Thickness with Time. *Geotechnique, 8*, 171-182.

Gordon, D. S. & Flemings, P. B. (1998). Generation of Overpressure and Compaction-Driven Fluid Flow in a Plio-Pleistocene Growth-Faulted Basin, Eugene Island 330, Offshore Louisiana. *Basin Research, 10*, 177-196.

Ham, H. H. (1966). A Method of Estimating Formation Pressure from Gulf Coast Well Logs. *Transactions - Gulf Coast Association of Geological Societies, 16*, 185-196.

Harrison, W. & Summa, L. (1991). Paleohydrology of the Gulf of Mexico Basin. *American Journal of Science, 291*, 109-176.

Hart, B. S., Flemings, P. B., & Deshpande, A. (1995). Porosity and Pressure: Role of compaction disequilibrium in the development of geopressures in a Gulf Coast Pleistocene basin. *Geology, 23,* 45-48.

Holman, W. E., & Robertson, S. S. (1994). Field Development, Depositional Model, and Production Performance of the Turbiditic "J" Sands at Prospect Bullwinkle, Green Canyon 65 Field, Outer-Shelf Gulf of Mexico. In *GCSSEPM Foundation 15th Annual Research Conference, Submarine Fans and Turbidite Systems, 4-7 December,* 139-150.

Ingram, G.M. & Urai, J.L. (1997). Top Seal Leakage Through Faults and Fractures: the role of mudrock properties. In *Proceedings of the Geological Society Conference on "Mudrocks at the Basin Scale: Properties, Controls and Behavior", 28-29 January,* 1-30.

Issler, D. (1992). A New Approach to Shale Compaction and Stratigraphic Restoration, Beaufort-Mackenzie Basin and Mackenzie Corridor, Northern Canada. *American Association of Petroleum Geologists Bulletin, 76,* 1170-1189.

Kikani, J. & Smith, T. (1996). Recovery Optimization and Modeling Depletion and Fault Block Differential at Green Canyon 110. *Society of Petroleum Engineers, Paper 36693,* 157-170.

Kooi, H. (1997). Insufficiency of Compaction Disequilibrium as the Sole Cause of High Pore Fluid Pressures in Pre-Cenozoic Sediments, *Basin Research, 9,* 227-242.

Lupa, J.A., Flemings, P.B. & Tennant, S. (2002). Pressure and Trap Integrity in the Deep-water Gulf of Mexico. *The Leading Edge, 21*(2), 184-187.

Mann, D.M. & Mackenzie, A.S. (1990). Prediction of Pore Fluid Pressures in Sedimentary Basins. *Marine and Petroleum Geology, 7,* 55-65.

Malin, M.C., & Edgett, K.S. (2000). Evidence for Recent Groundwater Seepage and Surface Runoff on Mars. *Science, 288,* 2330-2335.

Neuzil, C. E. (1994). How Permeable are Clays and Shales? *Water Resources Research, 30*(2), 145-150.

O'Connell, J. K., Kohli, M., & Amos, S. (1993). Bullwinkle: A unique 3-D experiment. *Geophysics*, *58*(1), 167-176.

Ostermeier, R. M., Pelletier, J. H., Winker, C. D., Nicholson, J. W., Rambow, F. H., & Cowan, K. M. (2000). Dealing with Shallow-Water Flow in the Deepwater Gulf of Mexico. In *2000 Offshore Technology Conference, Paper 11972.*

Phillips, O.M. (1991). *Flow and Reactions in Permeable Rocks*. New York, Cambridge University Press, 285 p.

Pilkington, P.E. (1978). Fracture Gradient Estimates in Tertiary Basins. *Petroleum Engineer International, 8*(5), 138-148.

Plumley, W. J., 1980. Abnormally High Fluid Pressure: Survey of some basic principles. *The American Association of Petroleum Geologists, 64*(3), 414-422.

Revil, A., Cathles, L. M. III, & Shosa, J. D. (1998). Capillary Sealing in Sedimentary Basins; a clear field example. *Geophysical Research Letters, 25*(3), 389-392.

Rowan, M.G. (1995). Structural Styles and Evolution of Allochthonous Salt, Central Louisiana Outer Shelf and Upper Slope. In M.P.A. Jackson, D.G. Roberts, and S. Snelson (Eds.), *Salt tectonics: A global perspective, AAPG Memoir, 65,* 119-225.

Rowan, M.G., Jackson, P.A. & Trudgill, B.D. (1999). Salt-Related Fault Families and Fault Welds in the Norhthern Gulf of Mexico. *AAPG Bulletin, 83*(9), 1454-1484.

Rubey, W. W. & Hubbert, M. K. (1959). Role of Fluid Pressure in mechanics of Overthrust Faulting. *Bulletin of the Geological Society of America, 70,* 167-206.

Saffer, D., Silver, E., Fisher, A., Tobin, H. & Moran, K. (2000). Inferred Pore Pressures at the Costa Rica Subduction Zone: Implications for dewatering processes. *Earth and Planetary Science Letters*, *177*(3-4), 193-207.

Schowalter, T.T. (1976). The Mechanics of Secondary Hydrocarbon Migration and Entrapment. *The Wyoming Geological Association Earth Sciences Bulletin*, *9*(4), 1-43.

Stump, B. (1998). Illuminating Basinal Fluid Flow in Eugene Island 330 (Gulf of Mexico) Through In Situ Observations, Deformation Experiments, and Hydrodynamic Modeling. Masters Thesis, Penn State University, 121 p.

Stump, B. & Flemings, P. B. (2000). Overpressure and Fluid Flow in Dipping Structures of the Offshore Gulf of Mexico (E.I. 330 Field). *Journal of Geochemical Exploration*. *69-70*, 23-28.

Stump, B. & Flemings, P.B. (2002). Consolidation State, Permeability, and Stress Ratio as Determined from Uniaxial Strain Experiments on Mud Samples from the Eugene Island 330 Area, Offshore Louisiana.in A.R. Huffman and G.L. Bowers (Eds.), *Pressure Regimes in Sedimentary Basins and Their Prediction, AAPG Memoir, 76,* 131-144.

Styzen, M. J. (1996). A Chart in Two Sheets of the Late Cenozoic Chronostratigraphy of the Gulf of Mexico. *Guilf Coast Section, Society of Economic Paleontologists and Mineralogists,* Houston, Texas.

Swanston, A.M. (2001). Imaging Drainage of Turbidite Reservoirs Through Time-Lapse Seismic Analysis at Bullwinkle, Green Canyon Block 65, Offshore Gulf of Mexico. Masters Thesis, Penn State University, 112 p.

Swanston, A.M., Flemings, P.B., Comisky, J.T. & Best, K.D. (in press). Time-Lapse Imaging at Bullwinkle, GC 65. Offshore Gulf of Mexico, *Geophysics.*

Traugott, M. (1996). The Pore Pressure Centroid Concept: Reducing drilling risks. In *Abstract: Compaction and Overpressure in Current Research, 9-10 December, IFP, Paris.*

Winker, C.C. & Booth, J.R. (2000). Sedimentary Dynamics of the Salt-Dominated Continental Slope, Gulf of Mexico: Integration of Observations from teh Seafloor, Near-Surface, and Deep Subsurface. In *GCSSEPM Foundation 20th Annual Research Conference, Deep-Water Reservoirs of the World, 3-6 December,* 1059-1086.

Yardley, G.S. & Swarbrick, R.E. (2000). Lateral Transfer: A source of additional overpressure? *Marine and Petroleum Geology, 17,* 523-537.